

1

2 **Fault slip potential induced by fluid injection in the**
3 **Matouying EGS field, Tangshan seismic region, North**
4 **China**

5 **Chengjun Feng^{1,2}, Guangliang Gao^{3,4}, Shihuai Zhang⁵, Dongsheng Sun^{1,2}, Siyu**
6 **Zhu¹, Chengxuan Tan^{1,2}, Xiaodong Ma⁵**

7

8 ¹Institute of Geomechanics, Chinese Academy of Geological Sciences, Beijing, 100081, China

9 ²Key Laboratory of Active Tectonics and Geological Safety, Ministry of Natural Resources, Beijing,
10 100081, China

11 ³China University of Petroleum, Qingdao, 266580, China

12 ⁴Jidong Oilfield Company, PetroChina, Tangshan, 063000, China

13 ⁵Department of Earth Sciences, ETH Zürich, Zürich, 8092, Switzerland

14

15 **Correspondence:** Chengjun Feng (feng2010618@aliyun.com)

16

17 **Abstract.** The Tangshan region is one of the most seismically active areas in the North China, and
18 the 1976 M 7.8 earthquake occurred on July 28th near the Tangshan fault zone. The Matouying
19 Enhanced Geothermal System (EGS) field is located ~90 km away from Tangshan City. Since the late
20 2020, preliminary hydraulic stimulation tests have been conducted at depths of ~3965–4000 m. Fluid
21 injection into geothermal reservoir facilitates heat exchanger system. However, fluid injection may also
22 induce earthquakes. In anticipation of the EGS operation at the Matouying uplift, it is essential to
23 assess how the fault slip potential of the nearby active and quiescent faults will change in the presence
24 of fluid injection. In this study, we first characterize the ambient stress field in the Tangshan region by
25 performing stress tensor inversions using 98 focal mechanism data ($M_L \geq 2.5$). Then, we estimate the
26 principal stress magnitudes near the Matouying EGS field by analyzing in situ stress measurements at
27 shallow depths (~600–1000 m). According to these data, we perform a quantitative risk assessment
28 using the Mohr-Coulomb framework in order to evaluate how the main active faults might respond to
29 hypothetical injected-related pore pressure increases due to the upcoming EGS production. Our results
30 mainly show that most earthquakes in the Tangshan seismic region have occurred on the faults that
31 have relatively high fault slip potential in the present ambient stress field. At well distances of less than
32 15 km, the probabilistic fault slip potential on most of the boundary faults increase with continuing
33 fluid injection over time, especially on these faults with well distances of ~6–10 km. The probabilistic
34 fault slip potential (FSP) increases linearly with the fluid injection rate. However, the FSP values
35 decrease exponentially with increased unit permeability. The case study of the Matouying EGS field
36 has important implications for the deep geothermal exploitation in China, especially for Gonghe EGS
37 (in Qinghai province) and Xiong'an New Area (in Hebei province) geothermal reservoirs that are close

1 to the Quaternary active faults. Ongoing injection operations in the regions should be conducted with
2 these understandings in mind.

3 **1 Introduction**

4 Enhanced geothermal systems (EGS) are a promising source of renewable energy for a decarbonizing
5 world and can provide a valuable contribution to the production of renewable energy (Lee et al., 2019).
6 The EGS technologies exploit geothermal resources through hydraulic stimulation, which involves the
7 injection of high-pressure cold water into the target formation in order to increase the unit permeability
8 by creating new fractures or causing preexisting fractures to widen (Terakawa et al., 2012; Grigoli et al.,
9 2018; Lee et al., 2019). To economically produce electricity and heat with an EGS, it is necessary to
10 employ an efficient hydraulic subsurface heat exchanger system that can circulate through the hot rock
11 that hosts the permeable fracture network (Bromley et al., 1987; Häring et al., 2008).

12 The industrial process of hydraulic stimulation involves creating tensile fractures and
13 subsequently increasing the permeability of the target rock formations via the controlled injection of
14 pressurized fluid (Ellsworth, 2013). However, while the injection of fluid into reservoir rocks facilitates
15 oil and gas recovery, plays a key role in EGS, and aids in the disposal of wastewater and CO₂ gas, fluid
16 injection may also induce earthquakes (Shapiro et al., 2005; Evans et al., 2012; Zoback and Gorelick,
17 2012; Ellsworth, 2013; Zang et al., 2014; McGarr et al., 2015; Walsh and Zoback, 2015; Lei et al., 2017;
18 Kim et al., 2018; Lee et al., 2019). Seismic events caused by fluid injection are a possible hazard faced
19 by nearly all engineering endeavors that result in changes to the ambient subsurface stress or pore
20 pressure (Evans et al., 2012).

21 For the past 40 years, induced seismicity has been documented in geothermal settings such as the
22 Philippines (Bromley et al., 1987), Japan (Nagana et al., 1994), Kenya (Simiyu, 1999), North and
23 South America (Henderson et al., 2002), Australia (Baisch et al., 2006), and New Zealand (Hunt and
24 Latter, 1982). Evans et al. (2012) compiled a survey of induced seismic events caused by fluid injection
25 in European geothermal reservoirs. Annually, thousands of seismic events (with local magnitudes $M_L <$
26 2.0) are generated during the exploitation of geothermal fields (Evans et al., 2012). Furthermore, EGS
27 case studies have demonstrated that injecting water into basement rock mass may also produce large
28 earthquakes (with moment magnitude $M \geq 3.0$). For example, in 2006 and 2007, four $M 3.0$ earthquakes
29 were caused by the high-pressure injection of water into impermeable basement rocks beneath Basel,
30 Switzerland (Deichmann and Giardini, 2009; Terakawa et al., 2012; Ellsworth, 2013; McGarr et al.,
31 2015). In 2017, a $M 5.5$ earthquake occurred near an EGS drill site in Pohang, South Korea (Zang et al.,
32 2014; Kim et al., 2018; Grigoli et al., 2018; Lee et al., 2019; Woo et al., 2019). Geological and
33 geophysical data from this study area suggests that the Pohang earthquake was caused by the injection
34 of fluid directly into the near-critically stressed Yangsan fault zone (Kim et al., 2018; Grigoli et al.,
35 2018).

36 On June 30th, 2019, the No. 2 Exploration Team of the Hebei Bureau of Coal Geological
37 Exploration in China announced that their team had drilled to a depth of 3965 m into the Matouying
38 (MTY) uplift (Fig. 1). With a temperature of 150°C, this area of hot dry rock is located ~90 km away
39 from Tangshan City in northern China (Qi et al., 2020; Zhang et al., 2020). At the time, geological

1 prospecting surveys indicated that the two target areas for the MTY EGS field had areas of 80 km² (at a
2 depth of 4000 m) and 500 km² (at a depth of 5000 m) and may yield as much as equivalent of ~2.8
3 billion and ~22.8 billion tons of standard coal, respectively. In 2020, preliminary hydraulic stimulation
4 tests were conducted at depths of ~3965–4000 m (Qi et al., 2020).

5 The Tangshan region is one of the most seismically active areas in the North China basin (Jiang,
6 2006; Feng et al., 2019). On July 28th, 1976, a *M*7.8 earthquake (focal depth of 10 km) struck the city
7 of Tangshan in northern China, 160 km east of Beijing City (Fig.1) (Guo et al., 1977; Chen et al., 1979).
8 The largest aftershock (the *M* 7.1 Luanxian earthquake) occurred on the same day approximately 45 km
9 northeast of the mainshock location (Fig. 1). Another large aftershock (the *M* 6.9 Ninghe earthquake)
10 near Ninghe County occurred on November 15th, 1976 (Fig. 1) (Nábělek et al., 1987; Huang and
11 Yeong, 1997). The Tangshan *M* 7.8 earthquake, which was one of the most devastating earthquakes in
12 the last 100 years worldwide, was responsible for more than 242,000 deaths and 800,000 injuries, and
13 ultimately destroyed the city of Tangshan (Li et al., 2018). Northern China is marked by unusually
14 active intraplate seismicity and Quaternary tectonic movement (Ye et al., 1985; Nábělek et al., 1987).
15 Previous studies indicate that most faults in the Tangshan seismic region, such as the Tangshan fault
16 belt, the Luanxian-Laoting fault, the Changli-Ninghe fault, and the Jiyunhe fault, were created by late
17 Pleistocene-Holocene tectonic activity (Li et al., 1998; You et al., 2002; Jiang, 2006; Guo and Zhao,
18 2019). While the seismic activity in the Tangshan region has decreased over the past 40 years (Zhang et
19 al., 2017), some *M*_L 4.0–5.0 earthquakes have still occurred in the past 10 years (e.g., 5/28/2012 (*M*_L
20 5.2), 9/14/2015 (*M*_L 4.2), 9/10/2016 (*M*_L 4.2), 3/24/2017 (*M*_L 4.4), 8/2/2019 (*M*_L 4.4)) (Yang et al., 2016;
21 Lin et al., 2017; Feng et al., 2019; Fan et al., 2019).

22 In anticipation of the EGS operation at the MTY uplift in the Tangshan seismic region, it is
23 essential to assess how the fault slip potential of the nearby active and quiescent faults will change in
24 the presence of fluid injection. In this study, we first characterize the ambient stress field in the
25 Tangshan region by performing stress tensor inversions using focal mechanism data (*M*_L≥2.5) from the
26 past 14 years. With these inversions, we determine the principal compressive stress orientations, the
27 prevailing stress regime, and the critical coefficients of friction throughout our study area. By analyzing
28 in situ stress measurements at shallow depths (~600–1000 m) in the Tangshan seismic region (Tan et al.,
29 2014; Tan et al., 2015; Niu et al., 2015; Feng et al., 2019), we estimate the principal stress magnitudes
30 near the MTY EGS field. We then perform a quantitative risk assessment using the Mohr-Coulomb
31 framework in order to evaluate how the main active faults in the Tangshan seismic region might
32 respond to hypothetical injected-related pore pressure increases due to the upcoming MTY EGS
33 production. This assessment is based on the FSP v.1.0 software package from Stanford Center for
34 Induced and Triggered Seismicity of Stanford University (Walsh and Zoback, 2015; Walsh and Zoback,
35 2016; Lund Snee and Zoback, 2018). In our analysis, we use only publicly available information
36 related to the most active faults in the Tangshan seismic region. Finally, we conduct a seismic hazard
37 assessment by predicting the maximum moment magnitudes of injection-induced seismic events in the
38 MTY EGS field in response to different net fluid injection volumes.

39 **2 Tectonics and seismicity in the Tangshan seismic region**

1 The Tangshan seismic region is situated in the northern part of the North China Plain. This large basin
2 began to form in the early to middle Eocene (Ye et al., 1985). As with many other basins, rifting was
3 the primary mode of tectonic activity in the initial stages of basin development (Shedlock et al., 1987).
4 This basin is bounded to the north by Yanshan Mountains and to the east and the south by Bohai Bay.
5 The topography is higher in the northern part of the basin than it is in the southern part of the basin
6 (Guo and Zhao, 2019) (Fig. 1). Structurally, the Tangshan seismic region is a part of the Kailuan
7 sag-fold system in the Yanshan fold belt; the basement material is the NE-trending Kaiping
8 synclinorium, a Yanshan stage formation that consists of Paleozoic rocks (Guo et al., 2011).
9 Geophysical prospecting (Hao et al., 1998; Li et al., 1998; Li et al., 2009; Yang et al., 2010; Liu et al.,
10 2011; Ran et al., 2013; Zhang et al., 2013), geological mapping (Zheng et al., 1981; Gao et al., 2001;
11 Guo et al., 2011; Guo and Zhao, 2019), and identification of geomorphic features (Qiu et al., 2005)
12 have revealed the existence of various fault systems in this region (Fig. 1); the orientations of these
13 fault systems are NEN (e.g., the Lulong fault - F_6), ENE (e.g., the Tangshan fault belt - F_4 , the Ye'jituo
14 fault - F_3 , the Changli-Ninghe fault - F_5 , the Cangdong fault - F_{14} , and the Xi'nanzhuang fault - F_{11}),
15 NW (e.g., the Ji'yunhe fault - F_2 , the Luanxian-Laoting fault - F_7 , and the Bai'gezhuang fault - F_8),
16 WNW (e.g., the Lengkou fault - F_{17}) and nearly EW (e.g., the Han'gu fault - F_{13} and the Haihe fault -
17 F_{12}). The NE-trending faults, which are the most prominent faults in the area, run throughout the entire
18 length of the Tangshan seismic region (Ye et al., 1985). Some of the faults sets (F_2 , F_3 , F_4 , F_5 , and F_7)
19 divide the basin into rhombic and triangular blocks. Furthermore, these faults show signs of recent
20 normal and strike-slip movement (Nábělek et al., 1987; Liu et al., 2011; Feng et al., 2019).

21 Based on the co-seismic crustal deformation, previous studies have concluded that the mainshock
22 of the 1976 M 7.8 Tangshan earthquake sequence ruptured along a right-lateral fault with a strike of
23 $N30^{\circ}$ – 53° E and a dip of 76° – 89° SE (Butler et al., 1979; Wan et al., 2017). The Luanxian M 7.1
24 earthquake was associated with pure normal faulting on a plane with a strike of $N30^{\circ}$ W and a dip of
25 45° – 53° NE (Huang and Yeong, 1997; Wan et al., 2017). The Ninghe M 6.9 earthquake was
26 characterized by left-lateral strike-slip faulting with a small normal component on a NW-striking
27 ($N36^{\circ}$ W) fault plane with a dip of 67° NE (Huang and Yeong, 1997; Wan et al., 2008; Wan et al.,
28 2017).

29 **3 Methodology**

30 The Mohr-Coulomb failure criteria is a useful framework for understanding how increasing the pore
31 fluid pressure via fluid injection can trigger seismic slip (Hubbert and Rubey, 1959; Healy et al., 1968;
32 Jaeger et al., 2007; Zoback and Gorelick, 2012; Walsh and Zoback, 2015; Walsh and Zoback, 2016).
33 Because of the critically stressed nature of the crust, a given fault will remain in a locked state as long
34 as the applied shear stress is lower than the strength of the contact (Hubbert and Rubey, 1959). The
35 critical shear stress is the product of the coefficient of friction and the effective normal stress given by
36 the difference between the applied normal and the pore pressure (Hubbert and Rubey, 1959; Raleigh et
37 al., 1976; Byerlee, 1978). Then, the critical shear stress on the earthquake fault under static friction is
38 given by the following expression:

$$\begin{aligned} 1 \quad & \tau_c = \mu(\sigma_n - P_f) \\ & P_f = P_0 + \Delta P \end{aligned} \quad (1)$$

2 where τ_c is the critical shear stress (MPa), σ_n is the normal stress (MPa), P_f is the total pore pressure
3 (MPa), μ is the coefficient of friction, P_0 is the natural pore pressure (MPa), and ΔP is the increasing
4 pore pressure (MPa) via fluid injection.

5 In ambient conditions, the effective normal stress, which is oriented normal to the plane of the
6 fault, effectively clamps the fault closed and reduces the likelihood of slip occurring on the fault.
7 During fluid injection, as the pore fluid pressure increases, the effective normal stress decreases
8 proportionally; this reduction in the normal stress unclamps the fault and may result in slip along
9 preexisting subcritical ruptures (Jaeger et al., 2007; Langenbruch and Shapiro, 2015; Walsh and Zoback,
10 2015).

11 Fluid injection in deep wells can trigger earthquakes when the injection causes the pore pressure
12 to increase near preexisting potentially active faults (Rutledge et al., 2004; Zoback and Gorelick, 2012;
13 Catalli et al., 2013). In these near-critical pressure conditions, relatively small perturbations to the
14 ambient pore fluid pressure conditions can and do trigger earthquakes; the Basel and Pohang events are
15 examples of earthquakes that were triggered by insignificant stress perturbations caused by fluid
16 injection (Terakawa et al., 2012; Walter et al., 2015; Kim et al., 2018; Woo et al., 2019).

17 Injection of fluids into a porous medium causes an increase in pore pressure that decays
18 exponentially with radial distance from the injection source. This pressure change radiates away from
19 the well axisymmetrically as injection continues; as such, the model calculates a radially symmetric
20 pressure profile for each injection well at a given time using Eqs. (2) and (3) (Ferris et al., 1962; Bear,
21 1979; Hsieh and Bredehoeft, 1981):

$$22 \quad T \left(\frac{\partial^2 h}{\partial x^2} + \frac{\partial^2 h}{\partial y^2} \right) = S \frac{\partial h}{\partial t} - Q(t) \delta(x) \delta(y) \quad (2)$$

$$\Delta P = rh$$

$$h(x, y, t) = \frac{Q(t)}{4\pi T} W(u) \left[\frac{(x^2 + y^2)S}{4Tt} \right]$$

$$23 \quad W(u) = \int_u^\infty \frac{e^{-u}}{u} du \quad (3)$$

$$u = R^2 \frac{S}{4Tt}$$

24 where h is the vertically averaged buildup of hydraulic head above the initial head (m), T is the
25 principal value of the transmissivity (m^2/s), S is the storage coefficient, $Q(t)$ is the variable injection
26 rate (L/s), r is the specific weight of the fluid (N/m^3), ΔP is the vertically averaged pressure increase
27 (MPa), $W(u)$ is the well function, and R is the radius distance away from the injection well (m).

28 These groundwater flow equations describe the two-dimensional (2D) radial flow in a vertically
29 confined aquifer containing a variable injection rate well. The idealized model of the reservoir makes
30 several simplifying assumptions to compute pressure buildup and the subsequent falloff caused by fluid
31 injection (Ferris et al., 1962; Papadopoulos, 1965; Bear, 1979; Hsieh and Bredehoeft, 1981; Walsh et al.
32 2017): (1) the porous medium is fully saturated and has a uniform pressure distribution, (2) the
33 hydraulic head is the same everywhere before the injection, (3) injection wells are treated as point

1 sources in the 2D grid, (4) the permeability and porosity are constant and isotropic, and (5) interacting
2 pressure plumes are superimposed linearly. Using this hydrologic model, Hsieh and Bredehoeft (1981)
3 approximated the pressure buildup in response to injection of fluid wastes into the fractured
4 Precambrian crystalline bedrock beneath the Rocky Mountain Arsenal (RMA) near Denver triggered
5 earthquakes in the 1960's, and their results showed that the increase of fluid pressure triggered the
6 swarm of earthquakes at the RMA.

7 In this study, we utilize the FSP v.1.0 software package to estimate the slip potential on the active
8 faults throughout the Tangshan seismic region. The FSP program allows for either a deterministic or
9 probabilistic geomechanical analysis of the fault slip potential based on the Mohr-Coulomb failure
10 criteria. Both the deterministic and probabilistic geomechanical models rely on several simplifying
11 assumptions (Walsh et al., 2017): (1) the natural pore pressure and stress tensor are uniform across the
12 study area and linearly increase in magnitude with depth, (2) one of the principal stress vectors is
13 vertical, and (3) the stress state is determined by the relative magnitude of the vertical stress vector
14 (maximum, intermediate, or minimum, respectively). The FSP tool allows the user to estimate the
15 likelihood that the planar fault segments in question will be critically stressed within a local stress field.
16 When the ratio of the resolved shear stress to the normal stress reaches a specific failure criterion
17 (determined using the linearized Mohr-Coulomb failure envelope), the fault becomes critically stressed
18 (Lund Snee and Zoback, 2018). It should be noted that the FSP program does not predict earthquakes.
19 Instead, the FSP program assesses the cumulative conditional probability of slip occurring on known
20 faults, rather than quantifying the seismic hazard of a given fault (Walsh et al., 2017).

21 Despite some limitations, FSP provides a forward looking probabilistic screening tool for known
22 faults near injection operations. Using the FSP tool, Walsh and Zoback (2016) calculated the
23 conditional probability of slip on mapped faults in response to injection-related increases in pore
24 pressure in north-central Oklahoma (USA), where widespread injection of produced saltwater has
25 triggered thousands of small to medium-sized earthquakes; Lund Snee and Zoback (2018) estimated
26 the potential for slip on mapped faults across the Permian Basin of west Texas in response to
27 injection-related pressure changes at depth that might be associated with future oil and gas
28 development activities in the region. Hennings et al. (2019) conducted a probabilistic assessment of
29 fault slip potential on the regionally mapped faults in the hydrocarbon-producing Fort Worth Basin of
30 north-central Texas, coinciding spatiotemporally with injection of 2 billion barrels of wastewater into
31 deep aquifers.

32 **4 Present tectonic stress field in the Tangshan seismic region**

33 **4.1 Stress field inversion from earthquake focal mechanisms**

34 Michael (1987) developed a linearized stress field inversion scheme that can be solved by applying a
35 least-squares technique. Based on Michael's method, Vavryčuk (2014) proposed a new iterative stress
36 inversion technique (MATLAB software package STRESSINVERSE) that not only allows the user to
37 determine the stress and fault orientations, but also accurately calculates the shape ratio. Furthermore,
38 using the focal mechanism data, STRESSINVERSE allows the user to estimate the frictional

1 coefficients of the seismogenic faults. In this study, we used the STRESSINVERSE software package
2 to perform a crustal tectonic stress field inversion in the Tangshan seismic region. The shape ratio R
3 (Gephart and Forsyth, 1984) is expressed as:

$$4 \quad R = \frac{\sigma_1 - \sigma_2}{\sigma_1 - \sigma_3} \quad (4)$$

5 where σ_1 , σ_2 , and σ_3 represent the maximum, intermediate and minimum principal stress, respectively.

6 To resolve the spatial variations in the inversion stress regime, we use the regime stress ratio (RSR)
7 parameter defined by Simpson (1997):

$$8 \quad RSR = (n + 0.5) + (-1)^n (R - 0.5) \quad (5)$$

9 where n is equal to 0 for normal faulting (NF), 1 for strike-slip faulting (SS), and 2 for reverse faulting
10 (TF), respectively (Hergert and Heidbach, 2011).

11 An advantage of the RSR parameter is that it provides a continuous scale from pure normal
12 faulting ($RSR = 0.0$), normal/strike-slip faulting ($0.5-1.5$), pure strike-slip faulting ($RSR = 1.5$),
13 reverse/strike-slip faulting ($1.5-2.5$), and pure reverse faulting ($RSR = 2.5$) (Simpson, 1997).

14 Using full waveform data, Lin et al. (2017) determined the focal mechanisms of 918 earthquakes
15 ($M_L \geq 2.5$) that occurred between January of 2010 and June of 2014 in North China using the FOCMEC
16 (Sonke, 2009) and TDMT_ISO (Dreger and Helmberger, 1993; Minson and Dreger, 2008) methods. In
17 this massive data set, they identified 572 especially robust focal mechanisms. In our study, we used 75
18 focal mechanisms data ($M_L \geq 2.5$) from the Lin et al. (2017) data set that sample the Tangshan seismic
19 region (with latitudes of N 38.8°–N 40.4° and longitudes of E 117.2°–E 119.8°) as the input data for
20 our crustal tectonic stress field inversion. Moreover, we also used 23 focal mechanisms ($M_L \geq 3.0$) from
21 earthquakes that occurred between November of 2006 and November of 2009 (Huang and Wan, 2015;
22 Fan et al., 2019) and between November of 2015 and March of 2019 (Yang et al., 2016; Feng et al.,
23 2019). Our total Tangshan seismic region data set is comprised of 98 focal mechanisms ($M_L \geq 2.5$) that
24 occurred during 2006–2019 (Fig. 2 and Table S1). The focal mechanisms, which summarize the
25 prevailing sense of slip during a seismic event, are generally classified as thrust faulting (TF), normal
26 faulting (NF), normal faulting with a strike-slip faulting component (NS), thrust faulting with a
27 strike-slip faulting component (TS), or pure strike-slip faulting (SS) (Zoback, 1992).

28 Previous studies show that there are spatial stress variations in the Tangshan seismic region (Feng
29 et al., 2019). In order to investigate the crustal tectonic stress field in this area, we divide the Tangshan
30 seismic region into $0.1^\circ \times 0.1^\circ$ bins, where each bin contains at least one earthquake. With a confidence
31 interval of 95%, the results of the inversion in each bin include the predominant maximum principal
32 compressive stress orientation (σ_1), the regime stress ratio (RSR), and the frictional coefficient (μ).

33 **4.2 Present tectonic stress field in the Tangshan seismic region**

34 As shown in Fig. 3a, the Tangshan seismic region is characterized by local stress heterogeneity. The
35 maximum principal stress (σ_1) orientations of ENE-EW dominate the Tangshan seismic region, while
36 some WNW ($\sim 100^\circ-112^\circ$) σ_1 orientations occur near the Lulong fault (F_6) in Luanxian County. Zhang
37 et al. (2008) suggests that the σ_1 axis has orientations of $\sim 70^\circ-80^\circ$ (ENE), 91° (EW), and 91° (EW) in
38 the Tangshan, Ninghe, and northern Luanxian counties, respectively. While investigating the tectonic

1 field homogeneity in the Tangshan area, Yang et al. (2016) found that the σ_1 axes had orientations of
2 $\sim 87^\circ$ – 92° (ENE-EW) and 103° (WNW) near the Tangshan fault and the Lulong fault, respectively. Our
3 σ_1 axis results generally coincide with the those of previous studies (Zhang et al., 2008; Yang et al.,
4 2016). Furthermore, our regional tectonic stress field inversion, which was constrained using all 98
5 focal mechanisms (Fig. 3b), revealed that $N83^\circ E$ is the dominant σ_1 orientation in the Tangshan seismic
6 region; this result is also consistent with previous studies in our study area (Li et al., 1980; Huang and
7 Wan, 2015; Lin et al., 2017; Fan et al., 2019) and in northern China (Xu et al., 2008).

8 Additionally, Fig. 3a suggests that the predominant *RSR* values vary between 0.66 and 1.58; these
9 values coincide with a normal/strike-slip faulting stress regime. This stress regime is characterized by
10 significant strike-slip faulting in the western (e.g., in Tangshan, Fengnan, Fengrun, and Ninghe counties
11 with *RSR* values of ~ 1.10 – 1.60) and eastern (e.g., in Fu'ning, Changli, and Laoting counties with *RSR*
12 values of ~ 1.20 – 1.45) parts of the Tangshan seismic region. The prevailing stress regime in the central
13 Tangshan seismic region is characterized by normal faulting with a small component of strike-slip
14 faulting (e.g., in Tanghai, Luannan, and Luanxian counties with *RSR* values of ~ 0.55 – 0.85). These
15 stress regimes are consistent with both the fault rupturing that occurred during the 1976 Tangshan
16 earthquake sequence (Butler et al., 1979; Huang and Yeong, 1997; Wan et al., 2017) and the present
17 active features of the main seismogenic faults in this area (Jiang, 2006; Guo et al., 2011; Guo and Zhao,
18 2019).

19 Fig. 4 shows that the estimated friction coefficients near the main seismogenic faults mainly vary
20 between 0.4–0.6; the Tangshan fault belt, the Luanxian-Laoting fault, the Changli-Ninghe fault, the
21 Jiyunhe fault, and the Cangdong fault all have a friction coefficient of ~ 0.4 . Byerlee (1978)
22 summarized numerous laboratory experiments on different rock types and stated that at elevated
23 effective normal stresses (< 100 MPa), the corresponding friction coefficient fell in the range of
24 ~ 0.6 – 1.0 . Townend and Zoback (2000) suggested that the ratio of the maximum to minimum effective
25 stresses corresponds to friction coefficients ranging from 0.6 to 1.0; these values indicate a state of
26 crustal equilibrium. When it comes to assessing the fault slip potential, an empirical friction coefficient
27 of 0.6 is typically invoked as the critical value (Zoback and Healy, 1992; Zoback et al., 2003; Moeck et
28 al., 2009; Qin et al., 2015; Lund Snee and Zoback, 2016; Lee and Ong, 2018; Zhang and Ma, 2021).
29 However, because the prevailing friction coefficient in our study area (0.40) is lower than the empirical
30 critical value of 0.6, we infer the presence of some weaker seismogenic faults in the Tangshan seismic
31 region; this conclusion agrees with the low friction coefficients ($\mu = 0.21$ – 0.45) found in the Changli
32 area of the eastern Hebei province (Feng et al., 2017). Multiple studies have reported low friction
33 coefficients near strong earthquake seismogenic faults. For example, the San Andreas Fault system has
34 μ values of ~ 0.18 – 0.26 (Hickman and Zoback, 2004; Carpenter et al., 2012), the Yinxiu-Beichuan fault
35 (a branch of the Longmenshan fault zone in the eastern margin of the Tibetan Plateau) is characterized
36 by a μ value of 0.4 (Verberne and He, 2010), and the friction coefficients of ~ 0.2 – 0.5 are found in the
37 Yishu fault zone (a branch of the Tan-Lu fault zone in eastern China) (Li et al., 2019).

38 4.3 Hydraulic fracturing measurements in the MTY EGS field

39 Currently, there are no in situ stress measurements of the MYT EGS field. However, we performed

1 hydraulic fracturing at the Qian'An borehole (QABH, depth of 600 m), the Changli borehole (CLBH,
 2 depth of 600 m), and the Luanxian borehole (LXBH, depth of 1000 m) from 2009 to 2013 in the
 3 northern part of the MTY EGS field (Fig. 1). The QABH, CLBH, and LXBH boreholes are
 4 approximately 70 km, 55 km, and 30 km away from the MTY EGS field, respectively (Fig.1). The
 5 locations, rock types, and rock mass integrity of the QABH, CLBH, and LXBH boreholes are listed in
 6 Table 1. The in situ stress measurements derived from our hydraulic fracturing tests at three boreholes
 7 are shown in Table 2 (Tan et al., 2014; Tan et al., 2015; Niu et al., 2015; Feng et al., 2017; Feng et al.,
 8 2019). Based on these in situ stress measurements, we can estimate the magnitude of the principal
 9 stresses at shallow depths near the MTY EGS field.

10 Table 2 shows that the magnitudes of σ_H , σ_h and σ_v vary between 4.04–28.51 MPa, 3.75–19.46
 11 MPa, and 1.79–24.44 MPa, respectively, over a depth range of 67.5–922.44 m. The magnitudes of the
 12 horizontal principal stresses (σ_H and σ_h) and the natural pore pressure (P_0) increase with depth (Fig. 5a).
 13 From this data together, we used linear regressions to determine how principal stresses and the natural
 14 pore pressure vary with depth:

$$15 \quad \sigma_H = 0.0278H + 5.33 \quad R^2 = 0.6215 \quad (6)$$

$$16 \quad \sigma_h = 0.0183H + 2.69 \quad R^2 = 0.7973 \quad (7)$$

$$17 \quad P_0 = 0.01H \quad R^2 = 0.9980 \quad (8)$$

$$18 \quad \sigma_v = 0.0265H \quad (9)$$

19 where R^2 is the correlation coefficient.

20 The linear gradients of σ_H and σ_h are 0.0278 MPa/m and 0.0183 MPa/m near the MTY EGS region,
 21 respectively. These gradients are slightly larger than those found in northern China above a depth of
 22 4000 m (σ_H gradient of ~ 0.0229 – 0.0233 MPa/m and σ_h gradient of ~ 0.0162 – 0.0170 MPa/m) (Yang et
 23 al., 2012; Huang et al., 2013), suggesting that there is a higher stress accumulation in the Tangshan
 24 seismic region than there is throughout the rest of northern China (Niu et al., 2015; Feng et al., 2019).
 25 Because the three principal stresses have magnitudes of $\sigma_H > \sigma_v > \sigma_h$ below a depth of 328 m, we infer that
 26 this area is dominated by a strike-slip faulting regime (Fig. 5a). The stress state at shallow depths (<
 27 1000 m) is consistent with the results of the focal mechanism inversion performed at seismogenic
 28 depths in the Tangshan seismic region (Fig. 3).

29 The measured σ_H orientations vary from N47°W to N82°W (average of N65°±18°W) at borehole
 30 QABH (depth range of 184.10–590.32 m), from N55°E to N82°W (average of N75°±20°E) at borehole
 31 CLBH (depth range of 67.50–485.50 m), and from N60°W to N74°W (average of N68°±8°W) at
 32 borehole LXBH (depth range of 340.00–922.44 m). The average σ_H orientation for all three boreholes
 33 at shallow depths (< 1000 m) is N80°W (or 100°), which is similar to the predominant σ_1 axis
 34 orientation (N83°E) throughout the entire Tangshan seismic region (Fig. 3b, Fig. 5b).

35 Previous studies suggest that the customary vector approach, which involves averaging the
 36 orientation of the maximum principal stresses, may yield unreasonable results and violate the tensorial
 37 nature of the stress variable (Gao and Harrison, 2017). Using Eq. (A2) from Feng et al. (2020) and our
 38 in situ stress data (Table 2), we first calculate the two-dimensional stress tensors at similar depths in the
 39 x (east) - o - y (north) coordinate system and then determine the tensorial mean of these stress states
 40 (Table 3). Finally, we estimate the predominant orientation of the maximum horizontal principal stress

1 in different boreholes by applying the mean stress tensors to Eq. (6) from Feng et al. (2020). As shown
2 in Table 3, the predominant σ_H orientations are N86°E at a depth interval of 206.50–212.92 m, N86°E
3 at a depth interval of 340.00–365.50 m, and N85°E at a depth interval of 468.68–485.50 m. These
4 estimated σ_H orientations are consistent with the tectonic stress field generated by our focal mechanisms
5 inversion for the Tangshan area (N83°E) (Fig. 3b).

6 **5 Results**

7 **5.1 Deterministic fault slip potential in Tangshan seismic region under the present stress field**

8 Here, we use only publicly available information related to the most active faults in the Tangshan
9 seismic region. Based on the results of urban active fault explorations conducted in Tianjin City by the
10 Tianjin Earthquake Agency (Zheng et al., 2006; Chen et al., 2010; Liu et al., 2013; Yan et al., 2014) and
11 in the Hebei province of China conducted by the Hebei Earthquake Agency (Peng and Meng, 2017), we
12 collected location, length, strike, and dip information for the main active faults in the Tangshan seismic
13 region. The simplified strike data for various fault segments are shown in Fig. 6. This data set contains
14 53 fault segments, each defined by two connected coordinate points. The three-dimensional geometries
15 of the active faults used in the fault slip potential calculation are listed in Table 4.

16 We first apply the deterministic geomechanical function of the FSP tool to estimate the slip
17 potential of the main active faults in the Tangshan seismic region in the absence of fluid injection. As
18 shown in Eqs.(6) and (7), the maximum (σ_H) and minimum (σ_h) horizontal stress gradients are 0.0278
19 MPa/m and 0.0183 MPa/m, respectively. The vertical stress (σ_v) gradient is 0.0265 MPa/m and the
20 initial pore pressure (P_0) gradient is taken as 0.01 MPa/m (Fig. 5). The reference depth for these
21 calculations is 3965 m, which is the depth of the uppermost boundary of the MTY EGS. We used a
22 critical friction coefficient (μ) value of 0.4 (Fig. 4). The orientation of the maximum principal stress ,
23 N83°E (Fig. 3b), is also added to the stress database.

24 Fig. 7 shows the results of a deterministic geomechanical assessment of the fault pore pressure
25 required to generate fault slip across the Tangshan seismic region. We find that the active faults will not
26 all instantaneously slip in the present stress field and natural pore pressure conditions (Fig. 7a).
27 However, the deterministic pore pressures required to cause slip on each fault segment vary with the
28 different fault strikes (Fig. 7b). About 23% of the faults striking NE or WNW are likely to slip in
29 response to a small fluid pressure increase ($\Delta P = 2.58\text{--}4.93$ MPa); some of these more critical faults
30 include the F_{4-1} , F_{4-3} , and F_{4-6} segments of the Tangshan fault belt ($\Delta P = 2.58\text{--}2.85$ MPa), the F_{5-3} , F_{5-4} ,
31 and F_{5-8} segments of the Changli-Ninghe fault ($\Delta P = 3.25\text{--}4.93$ MPa), and the F_{17-1} , F_{17-2} , and F_{17-3}
32 segments of the Lengkou fault ($\Delta P = 4.49\text{--}4.72$ MPa) (Fig. 7c). Many (~49%) of the NE-ENE or
33 WNW striking faults are likely to slip in response to a modest pore pressure increase ($\Delta P = 5.40\text{--}10.70$
34 MPa); some examples of these faults include the Yejituo fault (F_3) (ΔP of ~5.47–6.15 MPa), the Haihe
35 fault (F_{12}) (ΔP of ~6.67–10.70 MPa), and the Qinbei fault (F_9) (ΔP of ~5.41–6.39 MPa) (Fig. 7c).
36 Nearly 19% of the faults will likely slip at a large pore pressure perturbation ($\Delta P = 12.38\text{--}19.54$ MPa);
37 an example of these less sensitive fault is the northwestern segment of the Baigezhuang fault (F_8) (Fig.
38 7c). The deterministic geomechanical assessment of the fault pore pressure required to generate slip are

1 listed in Table S2.

2 **5.2 Probabilistic fault slip potential in Tangshan seismic region under the present stress field**

3 Because the deterministic model ignores some uncertainties that are often present in the strike, dip,
4 ambient stress field, and the coefficient of friction (Walsh and Zoback, 2016; Lund Snee and Zoback,
5 2018), the deterministic geomechanical results are not entirely reliable. To minimize these uncertainties,
6 we use a probabilistic geomechanical function to estimate the fault slip potential (FSP) on each fault
7 segment using a Monte-Carlo-type analysis to randomly sample the specified uniform uncertainty
8 distributions for the input parameters (Lund Snee and Zoback, 2018). A Monte Carlo approach is useful
9 because it propagates the relevant uncertainties through the model, producing a distribution of pore
10 pressure values that may result in fault slip (Walsh et al., 2017).

11 Qin et al. (2014) suggested that the gradients of σ_H and σ_h with depth are 0.0328 MPa/m and
12 0.0221 MPa/m in and around the Beijing region, respectively. Huang et al. (2013) reported that the σ_H
13 and σ_h gradients in the Zhangjiakou-Beijing-Bohai tectonic belt are approximately 0.0228 MPa/m and
14 0.0159 MPa/m, respectively. Considering that our study area is located in the eastern Beijing region
15 and in the southeastern section of the Zhangjiakou-Beijing-Bohai tectonic belt, we infer that the linear
16 σ_H and σ_h gradients near the MTY EGS field may vary between 0.0228–0.0328 MPa/m and
17 0.0159–0.0221 MPa/m, respectively.

18 Based on these assumptions, we can apply reasonable values and uncertainty ranges for the
19 gradients of σ_H (0.0278±0.005 MPa/m) and σ_h (0.0183±0.0024 MPa/m) with depth. The fault strike and
20 dip angles have uncertainties of ±5° and ±10°, respectively, the coefficient of friction on each fault
21 segment varies from 0.35 to 0.45 (average of 0.40±0.05), and the direction of the σ_1 axis varies from
22 66° (ENE) to 100° (WNW) (average of 83°±17°). An example of this type of analysis is shown in Fig.
23 S1 for the Tangshan fault belt. The distribution of pressures required to cause slip on fault F_{4-1} is
24 evaluated by randomly sampling the uniform distributions (shown in red) of the input parameter
25 distributions for 1000 geomechanical models.

26 Fig. 8 shows the results of our probabilistic fault slip analysis in the absence of fluid injection for
27 2020 with respect to the locations of recent earthquakes (2009–2019) with the magnitudes of M 1.0–4.9
28 in the Tangshan seismic region (National Earthquake Data Center, China). It is noteworthy that most of
29 these earthquakes have occurred on mapped faults with relatively higher FSP values; for example, the
30 Tangshan fault belt (F_4) has a 31%–41% probability of fault slip, the Jiyunhe fault (F_2) has a 27%–37%
31 probability of fault slip, and the northeastern segments of the Changli-Ninghe fault (F_{5-7} , F_{5-8} , F_{5-9})
32 have a 23%–35% probability of fault slip (Fig. 8a). However, many earthquakes have also occurred on
33 mapped faults with lower FSP values; for example, the Lulong fault (F_6) and the northwestern end of
34 the Luanxian-Laoting fault (F_{7-1}) have only a 5% and 3% probability of fault slip, respectively (Fig.
35 8b).

36 As shown in Fig. S2, we find that the probability of the fault slip potential on mapped faults F_{6-1} ,
37 F_{6-2} , F_{7-1} , and F_{7-2} is very sensitive to the σ_H azimuth. In the present stress field with a σ_H orientation of
38 83°±17°, the FSP values on faults F_{6-1} , F_{6-2} , F_{7-1} , and F_{7-2} are inconsistent with the high number of
39 earthquakes observed in the Lulong basin (Fig. 8b); from this observation, we conclude that local stress

1 field variations are responsible for these moderate-small events. If the σ_H azimuth changes from
2 $83^\circ \pm 17^\circ$ to $55^\circ \pm 17^\circ$ in the Lulong basin, the probability of fault slip on faults F_{6-1} and F_{6-2} increases to
3 32%–34% (Fig. S3a). Additionally, if the σ_H azimuth changes from $83^\circ \pm 17^\circ$ to $120^\circ \pm 17^\circ$ in the Lulong
4 basin, the probability of fault slip on faults F_{7-1} and F_{7-2} increases to 24%–25% (Fig. S3b). Generally,
5 the results shown in Fig. S3 suggest that the complex local stress field in the Lulong basin heavily
6 influences the fault slip potential and the earthquake activity in this area. Using the focal mechanisms
7 from the 1982 Lulong $M6.2$ earthquake and its aftershocks, Li et al. (2006) investigated the local stress
8 field in the Lulong Basin. They found that the maximum principal stress (σ_1) axis orientation changed
9 to $N43^\circ E$ in the northern part of the Lulong Basin; this orientation is distinctly different from the
10 dominant orientation of the regional tectonic stress field in the Tangshan seismic region (ENE-EW).

11 **5.3 Fluid pore pressure perturbations caused by fluid injection in the MTY EGS field**

12 The MTY EGS field lies in the gneiss unit of the Bai'miaozi Series in the Dan'tazi Group of the
13 Archeozoic Erathem, and has an area of 80 km^2 at the depth of 4000 m (Qi et al., 2020; Zhang et al.,
14 2020). The thickness of preliminary hydraulic stimulation test is 35 m (depth range of 3965–4000 m)
15 (Wang et al., 2013; Zhang et al., 2014). As a further simplification, horizontal two-dimensional flow is
16 assumed. In addition, at the depth interval of 3965–4000 m, the gneiss are well compact and intact with
17 fewer pre-existing fractures (Zhang et al., 2022). In these respects, the MTY EGS unit can be taken as
18 an infinite and isotropic reservoir. Thus, the Hsieh and Bredehoeft's hydrology model (Eqs. (2) and (3))
19 should be acceptable for the MTY EGS field.

20 The necessary hydrological parameters are the injection formation thickness and the porosity and
21 permeability of the injection layer. The average pre-enhancement porosity of the gneiss in the MTY
22 EGS field is equal to 6.9% (Zhou, 2003; Cao, 2016). The fractured reservoir permeability is closely
23 related to the apertures of the fractures and the average spacing between fractures (Murphy et al., 1999).
24 The actual fracture aperture mainly ranges from 0.05 mm to 2 mm, while the fracture spacing usually
25 ranges from several meters to dozens of meters (Murphy et al., 1999; Sanyal and Butler, 2005). For a
26 parallel fracture set, the average reservoir permeability theoretically ranges from 1 mD to 100,000 mD
27 (Zeng et al., 2013). Based on data from the oil and gas industry, however, the fracture permeability
28 following enhancement generally falls in the range of 1–100 mD (Sanyal and Butler, 2005; Zeng et al.,
29 2013; Yue et al., 2015). Due to the lack of existing permeability measurements in the MTY EGS field,
30 we must rely on a reasonable estimate of the fracture permeability. In this study, we assume that the
31 average fracture permeability of the MTY EGS field in the presence of hydraulic stimulation is equal to
32 100 mD.

33 Five hypothetical injection wells with identical injection rates (W01, W02, W03, W04, and W05
34 in Fig. 6) are placed in the MTY EGS region. The injection well data describes the injection rate profile
35 of each well over time, from January 1st of 2020 to December 31st of 2050. Evans et al. (2012)
36 determined many injection parameters for large induced earthquakes that were caused by fluid injection
37 in geothermal and CO_2 reservoirs in Europe. Their results showed that the circulation injection rates
38 associated with the largest magnitude events ranged from 18–120 L/s, (average of 51 L/s). In this study,
39 we used a fluid injection rate of 51 L/s (with a fluid density of 1000 kg/m^3) to calculate the pore

1 pressure diffusion near the MTY EGS field.

2 Fig. 9 shows the fluid pressure perturbations from five injection wells linearly superposed onto the
3 mapped domain of the Tangshan seismic region in 2050. The increasing fluid pressure due to injection
4 into five wells varied between 0 and 11.56 MPa (Fig. 9a). Furthermore, the highest fluid pressure
5 increases occur within ~15–20 km from each injection well. However, beyond this range, the fluid
6 pressure perturbations induced by fluid injection quickly decay to zero (Fig. 9b). Figs. S4 and S5 also
7 show the fluid pressure perturbations from the five injection wells linearly superposed onto the mapped
8 domain in 2030 and 2040, respectively.

9 **5.4 Probabilistic fault slip potential in the Tangshan seismic region in response to fluid injection** 10 **in the MTY EGS field**

11 In this section, we use the FSP v.1.0 program to determine the probability of the fault slip potential
12 (FSP) on the mapped faults in the Tangshan seismic region via the Mohr-Coulomb mechanism, in
13 response to a fluid injected-related pore pressure increase in the MTY EGS field .

14 Fig. 10 presents the probabilistic FSP values in the presence of hypothetical fluid injection from
15 2030 to 2050. The detailed results are also listed in Table S3. A comparison of Figure 10 with the Fig. 8
16 (in 2020) suggests that the probabilistic fault slip potential on most of the active faults, such as the
17 Ji'yunhe fault (F_2), the Ye'jituuo fault (F_3), the Tangshan fault belt (F_4), the Lulong fault (F_6), and the
18 Xi'nanzhuang fault (F_{11}) do not exhibit any obvious changes from 2020 to 2050 because they are more
19 than 45 km away from the five injection wells (Table S3).

20 For the faults that are within ~30–45 km of the injection wells, such as the F_{5-4} and F_{5-5} segments
21 of the Changli-Ninghe fault, the probabilistic FSP values vary from 37% in 2020 to 38% in 2050 and
22 from 18% in 2020 to 19% in 2050, respectively (Fig. S6a). Similarly, the probabilistic FSP values for
23 the F_{7-4} and F_{7-5} segments of the Luanxian-Laoting fault vary from 26% in 2020 to 27% in 2050 and
24 from 32% in 2020 to 33% in 2050, respectively (Fig. S6b). Additionally, the probabilistic FSP values
25 on the F_{8-3} segment of the Bai'gezhuang fault changes from 23% in 2020 to 25% in 2050 (Fig. S6c),
26 while the FSP value does not change at all on the F_{11-2} and F_{11-3} segments of the Xi'nanzhuang fault
27 (Fig. S6d). Overall, the hypothetical fluid injections only weakly impact the probabilistic FSP values
28 for the mapped faults at distances greater than ~30–45 km away from the hypothetical injection wells
29 in the MTY EGS field.

30 **5.5 Probabilistic fault slip potential in the MTY EGS field due to fluid injection**

31 As mentioned previously, the FSP values for most active faults in the Tangshan seismic region
32 increased very little in response to sustained fluid injections from 2020 to 2050 because they were
33 located at distances greater than ~30–45 km away from the injection wells in the MTY EGS field.
34 Previous observations on injection-induced seismicity shows that large-scale, field-wide injections may
35 perturb faults and induce earthquakes at distances of ~30–40 km away from the wells (Keranen et al.,
36 2014; Goebel et al., 2017). Goebel and Brodsky (2018) suggested that fluid injection into sedimentary
37 rocks can lead to more large and distant earthquakes for a given volume of injection; this behavior
38 corresponds to a power law-like behavior for areas with distances from wells that exceed 15 km. As

1 such, we investigate the probabilistic FSP values for faults located within distances of ~15–20 km away
2 from the hypothetical injection wells in the MTY EGS field.

3 Previous work focusing on the seismic interpretation and the drilling strata for oil exploration have
4 revealed valuable information pertaining to the structures of the main boundary faults near the MTY
5 EGS field (≤ 20 km) (Zhou, 2003; Dong, 2011; Zhao, 2014). As shown in Fig. 11, the MTY EGS field
6 is located in the central Matouying uplift (II), where it is bounded to the north by the Bai'gezhuang
7 lower uplift (IV), to the south by the Shi'jiutuo depression (I), and to the northeast by the Laoting
8 depression (III and V). The boundary faults of these tectonic units (Fig. 11a), such as boundary faults
9 F_{b1} - F_{b6} between the Matouying uplift and the Shi'jiutuo depression and faults F_{b8} - F_{b14} between the
10 Matouying uplift and the Bai'gezhuang lower uplift, are mainly characterized as normal faults with
11 large dips (Fig. 11b). Based on these field studies, we have determined the locations, lengths, strikes,
12 and dips of the main boundary faults near the MTY EGS field. The various strikes of the 20 different
13 fault segments are shown in Fig. 11a. The three-dimensional geometries of these boundary faults that
14 are used to calculate the probabilistic FSP values are listed in Table 5. We also utilize the FSP v.1.0
15 program to estimate the probabilistic FSP values for these boundary faults using the same stress,
16 hydrology, and injection well conditions described previously.

17 Fig. 12 presents the probabilistic FSP values for the mapped faults near the MTY EGS field in
18 2020, 2030, 2040, and 2050. Fig. S7 shows the FSP changes that have occurred on certain main
19 boundary faults (e.g., F_{b4} - F_{b6} , F_{b7} , F_{b8} - F_{b10} , F_{b11} - F_{b14} , and F_{b16} - F_{b20} segments) throughout the period of
20 fluid injection. The detailed results are listed in Table S4. Our results suggest that with continuing fluid
21 injection over time, the probabilistic FSP values on the boundary faults near the MTY EGS field will
22 progressively increase, especially for those faults with well distances of less than 15 km. Additionally,
23 the magnitude of the FSP changes vary with the fault strike and the distance from the injection wells.
24 For example, the FSP values for F_{b11} , F_{b12} , and F_{b13} (NE orientation) closest to injection wells 03 and
25 04 (with well distances ≤ 6 km) vary from 38.5% in 2020 to 59.5% in 2050, from 29.5% in 2020 to
26 59.7% in 2050, and from 11.1% in 2020 to 35.1% in 2050, respectively (Fig. S7d). These faults have
27 the largest FSP changes between 2020 and 2050, with increases of 21%, 30.2%, and 24%, respectively.
28 However, the FSP values for faults F_{b4} (NE orientation) and F_{b5} (WNW orientation), which have
29 similar well distances of 6 km of from injection wells 01 and 02, have smaller increases, with FSP
30 values of 8.1% in 2020 and 25% in 2050 and 14.6% in 2020 and 30.5% in 2050, respectively (Fig. S7a).
31 The increase in the FSP values for faults F_{b4} and F_{b5} are 16.9% and 15.9%, respectively. For fault F_{b7} ,
32 which is 7.5 km away from injection well 02, the FSP value varies from 35.5% in 2020 to 47.8% in
33 2050 (Fig. S7b)

34 Generally, the growth in the FSP values decays as the well distance increases. For example, faults
35 F_{b7} and F_{b14} , which are ~6–10 km away from the injection wells, have FSP value increases of 11.8%
36 and 14.9% (Figs.S7b and d). Faults F_{b6} , F_{b9} , F_{b10} , F_{b15} , F_{b17} , F_{b18} , F_{b19} , and F_{b20} , which are ~10–15 km
37 away from the injection wells, have FSP value increases that fall between 4.1%–8.6% (Figs.S7a, c, e,
38 and f). Lastly, faults F_{b8} and F_{b16} , which are ~15–20 km away from the injection wells, have FSP value
39 increases of 2.9% and 2.0% (Figs.S7c and e). However, faults F_{b1} , F_{b2} , and F_{b3} , which have NE
40 orientations and well distances of ~6–10 km, have very small FSP value increases of 0.1%–2.0% in

1 2020 and 0.1%–3.6% in 2050. The lower FSP values on these faults likely indicate that faults with a
2 strike of NEN/NS experience additional fault stability and have higher fault strengths in the present
3 ambient stress field.

4 **6 Discussion**

5 **6.1 Effect of injection rate on the fault slip potential in the MTY EGS field**

6 The injection rates and volumes at single wells may be related to nearby earthquake activity (Walters et
7 al., 2015). Earthquakes are more commonly associated with injection wells with high fluid injection
8 rates (Weingarten et al., 2015). Furthermore, earthquakes tend to occur just after rapid increases in the
9 injection rate (Kim, 2013). The likelihood of triggering earthquakes depends largely on the rate at
10 which the pore pressure increases, rather than the absolute magnitude of the pore pressure (Alghannam
11 and Juanes, 2020). Moreover, high injection rates in neighboring wells can also cause a cumulative
12 effect in the form of a large pressure halo that could trigger slip on potentially active faults (Keranen et
13 al., 2014; Walters et al., 2015; Walsh and Zoback, 2015).

14 We calculated the FSP values for the fault segments that are closest to injection wells 01, 03, and
15 04 in 2030, 2040, and 2050 (F_{b11} , F_{b12} , F_{b13} , and F_{b14}) (Fig. 13), with different fluid injection rates
16 ranging from 0 to 120 L/s in 20 L/s increments. As shown in Fig. 13, we found that the FSP values for
17 these fault segments increase linearly with the fluid injection rate in 2030 (Fig. 13a), 2040 (Fig. 13b),
18 and 2050 (Fig. 13c); the regression coefficients R^2 vary between 0.961 and 0.999. Because the F_{b13}
19 fault segment has the smallest well distance of these four fault segments, this segment experiences the
20 largest increases in the FSP gradient (%) versus fluid injection rate (L/s); the gradient changes are
21 0.3857 in 2030, 0.5000 in 2040, and 0.5679 in 2050.

22 **6.2 Effect of permeability on the fault slip potential in the MTY EGS field**

23 As discussed previously, we calculated the FSP values for the F_{b11} , F_{b12} , F_{b13} , and F_{b14} fault segments in
24 response to hypothetical fluid injection near the MTY EGS field, assuming an average permeability of
25 100 mD. We must assume that there is some uncertainty in this permeability estimate. As such, we
26 recalculated the probabilistic FSP values for fault segments F_{b11} , F_{b12} , F_{b13} , and F_{b14} in 2030, 2040, and
27 2050, respectively, with permeability values ranging from 10 to 250 mD in 10 mD increments (Fig.
28 14).

29 We found that an enhanced permeability could weaken the FSP values for these four fault
30 segments in 2030, 2040, and 2050. Furthermore, the FSP values of the mapped faults decrease
31 exponentially with higher permeability values during fluid injection. Nevertheless, Cappa et al. (2018)
32 suggest that permeability enhancement has an important effect on the pressure diffusion and aseismic
33 slip growth during fluid injection. Their results reveal that a more pronounced permeability
34 enhancement results in a larger aseismic slip zone. Moreover, aseismic slip may play a significant role
35 in triggering distant earthquake sequences located outside the target reservoir (Wei et al., 2015). As
36 such, the permeability and aseismic slip zone should be considered when conducting the ongoing
37 seismic hazard assessment of a given region due to fluid injection.

6.3 Effect of porosity on the fault slip potential in the MTY EGS field

The porosity of the gneiss in the Matouying and Bai'gezhuang uplifts mainly vary between 4.2% and 9.6% , with an average value of 6.9% (Zhou, 2003). To further understand how porosity may influence the probabilistic FSP on the mapped faults near the MTY EGS field, we recalculate the FSP values for the F_{b11} , F_{b12} , F_{b13} , and F_{b14} fault segments in 2030, 2040, and 2050, respectively, with porosity values ranging from 4.2% to 9.6% in 0.9% increment (Fig.15). We find that the FSP values of segments F_{b11} , F_{b12} , F_{b13} , and F_{b14} do not have obvious changes ($\Delta\text{FSP} < 6\%$), with increasing porosity. This finding is well consistent with our previous results in the Rongcheng geothermal reservoir of Xiong'an New Area, North China (Zhu et al., 2022). In general, the fault slip potential on the mapped faults induced by long-term fluid injection in the MTY EGS field changes slightly in response to variations in porosity.

6.4 Effect of thermoelastic stress on the fault instability in the MTY EGS field

The influence of temperature has not been considered in the analyses although temperature-induced stresses may play a significant role during EGS stimulation (Ghassemi and Tao, 2016). As a thermally uncoupled case of heating of a half space, the temperature-induced horizontal stresses can be estimated using the solution provided by Cheng (2016):

$$\Delta\sigma_{horizontal} = \alpha_d \frac{1-2\nu}{1-\nu} \Delta T \quad (10)$$
$$\alpha_d = K\beta_d$$

where $\Delta\sigma_{horizontal}$ is the change in horizontal stress (MPa) with a change in temperature ΔT ($^{\circ}\text{C}$), α_d is a drained thermoelastic effective stress coefficient ($\text{MPa}/^{\circ}\text{C}$), β_d is a volumetric expansion coefficient ($^{\circ}\text{C}^{-1}$), K is the bulk modulus of the reservoir rock (MPa), ν is Poisson's ratio.

It is assumed that the temperature drop is uniform throughout the reservoir ($\sim 3965\text{--}4000$ m), and the average temperature will decline by 6°C during 20 years (Segall and Fitzgerald, 1998). The average Young's modulus E of the gneiss in the MTY EGS field is equal to 20 GPa and the Poisson's ratio ν is equal to 0.23 (Li and Dong, 2013). Therefore, the bulk modulus K [$K=E/3(1-2\nu)$] is equal to 12.35 GPa. A reasonable value for granitic gneiss can be calculated using β_d of $2.4\text{e}^{-5}^{\circ}\text{C}^{-1}$ (McTigue, 1990), resulting in the α_d of $0.296\text{ MPa}/^{\circ}\text{C}$. Then, the changes in horizontal stress is calculated for a temperature drop of 6°C with a value of 1.25 MPa.

Taking faults F_{b7} , F_{b11} , F_{b12} , F_{b13} , and F_{b14} as examples, we determined the fault stress state in the Mohr's circles in 2040, when the average temperature hypothetically decline by 6°C throughout the MTY geothermal reservoir. As shown in Fig.16, the black dot marks the traction of the fault instability without the influence of thermoelastic stress, while the red dot marks the traction of the fault instability with the effect of temperature-induced stress changes. Generally, the effect principal stresses σ_H and σ_h both decrease by 1.25 MPa at a depth of 3965 m. The decreasing thermoelastic stress on the selected faults in 2040 shifts the Mohr's circles to the left. The temperature drop-induced stresses play a slight effect on the fault instability on the faults F_{b7} , F_{b11} , F_{b12} , F_{b13} , and F_{b14} under a strike-slip faulting stress regime.

6.5 The predicted maximum magnitude of injection-induced seismicity in MTY EGS field

1 It is possible to estimate the maximum magnitude of earthquakes induced by fluid injection through
 2 statistical, analytical, or hybrid forecasting methods (Gaucher et al., 2015; Tharaka et al., 2020). In this
 3 study, our predictions are based on the recently developed and commonly accepted models proposed by
 4 McGarr (2014), Van der Elst et al. (2016), and Galis et al. (2017).

5 McGarr (2014) predicted the maximum magnitude of injection-induced earthquakes by simulating
 6 a fully-saturated reservoir with critically stressed and ideally oriented faults in the vicinity of an
 7 injection well. The model generates a linear relationship between the maximum magnitude and the net
 8 injected volume (ΔV):

$$9 \quad M_{\max} = G\Delta V \quad (11)$$

10 where G is the modulus of rigidity (MPa). This model is often used to estimate the upper bound of the
 11 seismic moment (M_{\max}) for planned injection activities with a single well or a set of wells.

12 Galis et al. (2017) also proposed a quantitative physics-based model to account for specific
 13 aspects of earthquake physics. The theoretical scaling relation between the largest magnitude of the
 14 earthquakes (M_0^{\max}) and the net injected volume (ΔV) can be expressed as:

$$15 \quad M_0^{\max} = \gamma \Delta V^{3/2} \quad (12)$$

$$\gamma = \frac{0.4255}{\sqrt{\Delta \tau_0}} \left(\frac{K\mu}{h} \right)^{3/2}$$

16 where $\Delta \tau_0$ is the background stress drop (MPa), K is the bulk modulus of the reservoir rock (MPa), μ is
 17 the friction coefficient, and h is the reservoir thickness (m).

18 If earthquakes follow a Gutenberg-Richter distribution, i.e., exponentially distributed in
 19 magnitude, and the total number of induced earthquakes is proportional to injection volume (ΔV). Van
 20 der Elst et al. (2016) derived an alternative expectation for the maximum magnitude M_{\max} based on
 21 sample size statistics. The maximum magnitude (M_{\max}) of induced earthquakes can be estimated as:

$$22 \quad M_{\max} = \frac{1}{b} (\Sigma + \lg \Delta V) \quad (13)$$

23 where b is the slope of the power law, Σ is the seismogenic index and is found to be relatively constant
 24 over the lifetime of the geothermal reservoir (Shapiro et al., 2010).

25 For the parameters used in Eq. (11), the average Young's modulus E of the gneiss in the MTY
 26 EGS field is equal to 20 GPa and the Poisson's ratio ν is equal to 0.23 (Li and Dong, 2013). Therefore,
 27 the modulus of rigidity G [$G=E/2(1+\nu)$] is equal to 8.13 GPa. For the parameters used in Eq. (12), the
 28 bulk modulus K is equal to 12.35 GPa, the background stress drop $\Delta \tau_0$ in the Tangshan seismic region is
 29 about 6 MPa (Xiao et al., 1992), the friction coefficient μ in this study is 0.4, and the reservoir
 30 thickness h of the MTY EGS is equal to 35 m (~3965–4000 m). In addition, for the parameters used in
 31 Eq. (13), the value of b is taken as 0.87 in Tangshen seismic region (Du et al., 2021). Being lack of the
 32 Σ at the MTY EGS sites, herein, we estimate the sample size prediction for maximum magnitude (Eq.
 33 (13)), using a hypothetical seismogenic index $\Sigma = -1.2$ at the geothermal systems in Cooper Basin,
 34 Australia (Shapiro et al., 2010).

35 Using these three models, we estimated the maximum magnitude of injection-induced seismic
 36 events within well distances of ~10–15 km in response to a monthly injection volume time series in the
 37 MTY EGS field (Fig. 17). Using common logarithm function, we then fit these calculated results to

1 obtain the relationship between the maximum moment magnitude (M_w) of injection-induced
2 earthquakes in response to a net injected volume (ΔV) in the MTY ESG field:

$$3 \quad M_w = 0.67 \times \lg^{\Delta V} + 0.66 \quad (14)$$

$$4 \quad M_w = 1.02 \times \lg^{\Delta V} - 0.48 \quad (15)$$

$$5 \quad M_w = 1.15 \times \lg^{\Delta V} - 1.38 \quad (16)$$

6 where Eqs. (14) and (15) are the best-fitting models generated using the methods of McGarr (2014) and
7 Galis et al. (2017), respectively. Eq.(16) is simplified from the model of Van der Elst et al. (2016) with
8 the b value of 0.87 and the Σ value of -1.2.

9 In these calculation, we used different monthly injection volume (V) ranging from $2.59 \times 10^3 \text{ m}^3$ to
10 $3.11 \times 10^5 \text{ m}^3$ and, corresponding to the fluid injected rate of $\sim 1 \text{ L/s} - 120 \text{ L/s}$. In addition, we also
11 considered the net injected volume (ΔV) as $10\%V$, $20\%V$, $30\%V$, and $40\%V$, respectively, due to the
12 fluid loss injected into the ESG reservoir (Table S5).

13 As shown in Fig. 17a, when the accumulated net injected volume is larger than 5000 m^3 , the
14 predicted M_w slowly increases from $M_w 3.1$ to $M_w 3.6$ using the McGarr model, from $M_w 2.9$ to $M_w 3.8$
15 using the Van der Elst model, and from $M_w 3.3$ to $M_w 4.1$ using the Galis model. The M_w estimations for
16 three models are relatively similar. The maximum predicted M_w for an injection-induced earthquake in
17 the MTY EGS field under an assumption of 10% fluid loss is $M_w 4.1$.

18 For a fluid loss of 20%, when the accumulated net injected volume surpasses 5000 m^3 , the
19 predicted M_w slowly increases from $M_w 3.1$ to $M_w 3.8$ with the McGarr model, from $M_w 2.9$ to $M_w 4.1$
20 with the Van der Elst model, and from $M_w 3.3$ to $M_w 4.4$ with the Galis model. In this scenario, the
21 maximum M_w of an injection-induced earthquake in the MTY EGS field is $M_w 4.4$ (Fig. 17b).

22 When the fluid loss is increased to 30% and the accumulated net injected volume is larger than
23 5000 m^3 , the predicted M_w slowly increases from $M_w 3.2$ to $M_w 3.9$ using the McGarr model, from M_w
24 2.9 to $M_w 4.3$ using the Van der Elst model, and from $M_w 3.5$ to $M_w 4.6$ using the Galis model. The
25 maximum M_w of an injection-induced earthquake is $M_w 4.6$ in these circumstances (Fig. 17c).

26 As shown in Fig. 17d, when the accumulated net injected volume is larger than 5000 m^3 and the
27 fluid loss is 40%, the predicted M_w slowly increases from $M_w 3.3$ to $M_w 4.0$ with the McGarr model,
28 from $M_w 2.9$ to $M_w 4.5$ with the Van der Elst model, and from $M_w 3.6$ to $M_w 4.7$ with the Galis model.
29 For 40% fluid loss, the maximum M_w of an injection-induced earthquake in the MTY EGS field is M_w
30 4.7 .

31 Previous studies indicate that 53 earthquakes ($M_w 2.0-2.7$) were caused by fluid injection
32 (injection volume of $\sim 300-360 \text{ m}^3/\text{day}$) in the Renqiu oilfield of North China from August to
33 November of 1986 (Fig. 20), and that 13 earthquakes ($M_w 2.0-3.5$) were caused by fluid injection
34 (injection volume of $\sim 300-390 \text{ m}^3/\text{day}$) from February to June of 1987 (Fig. 18) (Zhao and Yang,
35 1990).

36 To verify our predicted models (Eqs. 14, 15, and 16) for the maximum M_w of fluid
37 injection-induced earthquakes, we estimated the possible M_w of the injection-induced earthquake in the
38 Renqiu oilfield, which is located $\sim 310 \text{ km}$ away from the MTY EGS field. As shown in Fig. 18a, the
39 predicted maximum M_w of the injection-induced earthquakes that occurred between August and

1 November of 1986 using the McGarr model vary between 2.6 and 3.0 with an injected fluid loss of less
2 than 40%; these values are largely consistent with the observed earthquake magnitudes (M_w 2.0–2.7).
3 With the Galis model, the predicted maximum M_w of the injection-induced earthquakes that occurred
4 between February and June of 1987 vary between 2.5 and 3.3 (Fig.18b); these values are also
5 consistent with the recorded magnitudes of the actual earthquakes (M_w 2.0–3.5). With the Van der Elst
6 model, the predicted maximum M_w of the injection-induced earthquakes that occurred between
7 February and June of 1987 vary between 2.8 and 2.9 (Fig.18c); these values are slightly smaller than
8 the recorded magnitudes of the maximum earthquakes (M_w 3.5). By comparison, we find that the
9 maximum magnitudes of the injection-related seismicity estimated with the Galis model (M_w 3.3) are
10 slightly greater than the values by the McGarr model (M_w 3.0) and the Van der Elst model (M_w 2.9). In
11 addition, we also find that the maximum magnitudes of the injection-related seismicity estimated with
12 the Galis model (M_w 3.3) are more similar with the observed earthquake (M_w 3.5) in the Renqiu oil field,
13 North China.

14 In general, the difference in the expected maximum magnitudes estimated with three models is
15 less than 0.5. Based on this analysis, we conclude that these three of the predicted models shown in Eqs.
16 (14), (15) and (16) can be adopted to estimate the maximum moment magnitude of fluid-injected
17 seismic events in the MTY EGS field in anticipation of the upcoming EGS exploitation. As shown in
18 Fig.17, we find that the predicted maximum magnitude of earthquakes (M_w 4.7) induced by continuous
19 water injection for 30 days would be greatly smaller than that of the largest tectonic earthquake in
20 Tangshan seismic region (i.e., the 1976 M 7.8 earthquake).

21 7 Concluding Remarks

22 Our conclusions are as follows:

23 (1) At shallow depths, the linearly increasing gradients of the maximum (σ_H) and minimum (σ_h)
24 horizontal principal stresses near the MTY EGS field in the Tangshan seismic region of North China
25 are 0.0278 ± 0.005 MPa/m and 0.0183 ± 0.0024 MPa/m, respectively. The σ_H orientations vary from 66°
26 to 100° (average of $83^\circ \pm 17^\circ$) near the MYT EGS field.

27 (2) In the Tangshan seismic region, most earthquakes (M 1.0–4.9 from 2009 to 2019) have
28 occurred on the faults that, in the present tectonic stress field, have relatively high fault slip potentials.
29 For example, the Tangshan fault belt has FSP values ranging from 31% to 41%, and the Jiyunhe fault
30 belt has FSP values ranging from 27% to 37%. However, many earthquakes, such as those on the
31 Lulong fault and the northwestern end of the Luanxian–Laoting fault, have also occurred on faults with
32 lower FSP values (3%–5%). The existence of these seismic events likely indicates that there is a local
33 stress field with a σ_H orientation of $\sim 43^\circ$ – 55° in the Lulong basin.

34 (3) The linearly superimposed fluid pressure perturbations induced by continuous injection at five
35 hypothetical injection wells in the MTY EGS field do not exceed 12 MPa from 2020 to 2050 (average
36 fluid injection rate of 51 L/s). The fault segments that experience the highest fluid pressure
37 perturbations are those with well distances of ~ 15 – 20 km. However, beyond this range, the fluid
38 pressure perturbations induced by fluid injection rapidly decay to zero.

39 (4) When the well distance exceeds ~ 30 – 45 km in the MTY EGS field, the probabilistic fault slip

1 potential on most of the active faults does not change from 2020 to 2050 in the Tangshan seismic
2 region. At well distances of less than 15 km in the MTY EGS field, the probabilistic fault slip potential
3 on most of the boundary faults increase with continuing fluid injection over time, especially on faults
4 with well distances of ~6–10 km. For example, fault segments F_{b11} , F_{b12} , and F_{b13} between the
5 Bai'gezhuang lower uplift and the Matouying uplift have FSP values of 59.5%, 59.7%, and 35.1% in
6 2050, respectively.

7 (5) When we experiment with fluid injection rates (0 to 120 L/s) in our hypothetical wells, we find
8 that on fault segments F_{b11} , F_{b12} , F_{b13} , and F_{b14} , which are the fault segments with the shortest well
9 distances in the MTY EGS field, the probabilistic fault slip potential increases linearly with the fluid
10 injection rate. However, the FSP values on these faults decrease exponentially with increased unit
11 permeability during fluid injection.

12 (6) When the monthly injection volumes fall in the range of $\sim 2.59 \times 10^3$ – 3.11×10^5 m³ and the
13 injected fluid losses vary between ~10%–40%, the predicted maximum moment magnitude of an
14 injection-induced earthquake is M_w 4.1–4.7 in the MTY EGS field. The predicted maximum
15 magnitudes of injection-induced earthquakes would be smaller than that of the largest tectonic
16 earthquake in Tangshan seismic region.

17 (7) We show how the FSP software package can be used as a quantitative screening tool to
18 estimate the fault slip potential in a region with some uncertainties of the ambient stress field, and to
19 assess the reactivation potential on these faults of presumably higher criticality in response to fluid
20 injection. The case study of the MTY EGS field has important implications for the deep geothermal
21 exploitation in China, especially for Gonghe EGS (in Qinghai province) and Xiong'an New Area (in
22 Hebei province) geothermal reservoirs that are close to the Quaternary active faults. Ongoing injection
23 operations in the regions should be conducted with these understandings in mind.

24
25 *Author contributions.* CJ.F conceptualised the research, performed the tectonic stress field and fault slip
26 potential analysis, and wrote the manuscript. SH.Z conceptualised the research. GL.G implemented the
27 integrated seismic and geological data interpretation of the Matouying uplift and its vicinity. Both DS.S
28 and CX.T analyzed in situ stress measurements in the Tangshan seismic region. SY.Z estimated the
29 maximum magnitude of injection-induced seismicity in MTY EGS field. XD.M defined the research
30 structure and reviewed the manuscript.

31
32 *Competing interests.* The contact author has declared that neither they nor their co-authors have any
33 competing interests.

34
35 *Acknowledgments.* The authors wish to thank professor Quince Chen (Institute of Geomechanics, CAGS)
36 for providing in situ stress results measured at Luanxian borehole in Tangshan seismic region. We
37 would like to thank assistant professors Weifeng Sun, Peng Zhang and Bangshen Qi (Institute of
38 Geomechanics, CAGS) for conducting in situ stress measurements at Qian'an and Changli boreholes in
39 Tangshan seismic region. We also thank LetPub (www.letpub.com) for linguistic assistance and
40 pre-submission expert review.

1
2 *Financial support.* This research has been supported by the China Geological Survey (grant no.
3 DD20190317).

4 5 **References**

6 Alghannam, M., Juanes, R.: Understanding rate effects in injection-induced earthquakes, *Nature*
7 *Communications.*, 11, 3053, <https://doi.org/10.1038/s41467-020-16860-y>, 2020.

8 Baisch, S., Weidler, R., Vörös, R., Wyborn, D., and Graaf, L.D.: Induced seismicity during the
9 stimulation of a geothermal HFR reservoir in the Cooper Basin, Australia, *Bulletin of the*
10 *Seismological Society of America.*, 96,2242-2256, <https://doi.org/10.1785/0120050255>, 2006.

11 Bear, J.: *Hydraulics of Groundwater*, McGraw-Hill Book Company, New York.,1979.

12 Bromley, C.J., Pearson, C.F., Rigor, D.M., and PNOC-EDC.: Micoearthquakes at the puhagan
13 geothermal field, Philippines-A case of induced seismicity, *Journal of Volcanology and*
14 *Geothermal Research*, 31, 293-311, [https://doi.org/10.1016/0377-0273\(87\)90073-4](https://doi.org/10.1016/0377-0273(87)90073-4), 1987.

15 Butler, R., Stewart, G.S., and Kanamori, H.: The July 27, 1976 Tangshan, China earthquake-A
16 complex sequence of intraplate events, *Bulletin of the Seismological Society of America.*, 69,
17 207-220, 1979.

18 Byerlee, J.D.: Friction of rocks, *Pure and Applied Geophysics.*, 116, 615-626,
19 <https://doi.org/10.1007/BF00876528>, 1978.

20 Cao, K.X.: *Geological characteristics and stimulation technologies optimization for gneiss reservoir*,
21 *Beijing: China University of Petroleum (Beijing).*, 2016.

22 Cappa, F., Guglielmi, Y., Nussbaum, C., and Birkholzer, J.: On the relationship between fault
23 permeability increases, induced stress perturbation, and the growth of aseismic slip during fluid
24 injection, *Geophysical Research Letters.*, 45, 1-9, <https://doi.org/10.1029/2018GL080233>, 2018.

25 Carpenter, B.M., Saffer, D.M., and Marone, C.: Frictional properties and sliding stability of the San
26 Andreas fault from deep drill core, *Geology.*, 40, 759-762, <https://doi.org/10.1130/G33007>, 2012.

27 Catalli, F., Meier, M.A., and Wiemer, S.: The role of Coulomb stress changes for injection-induced
28 seismicity: The Basel enhanced geothermal system, *Geophysical Research Letters.*, 40, 72-77,
29 <https://doi.org/10.1029/2012GL054147>, 2013.

30 Chen, Y.K., Liu, F., Yuan, D., Li, W.D., Yang, X.L., and Gao, W.P.: Seismic risk quantitative
31 evaluation on blind faults in Tianjin area, *Seismology and Geology.*, 32, 138-149,
32 <https://doi.org/10.3969/j.issn.0253-4967.2010.01.014>, 2010.

33 Chen, Y.T., Huang, L.R., Lin, B.H., Liu, M.L., and Wang, X.H.: A dislocation model of the Tangshan
34 earthquake of 1976 from the inversion of geodetic data, *Acta Geophysica Sinica.*, 22, 201-217,
35 1979.

36 Cheng, A.: *Poroelasticity*, Springer Nature., 2016.

37 Deichmann, N., and Giardini, D.: Earthquakes induced by the stimulation of an Enhanced Geothermal
38 System below Basel (Switzerland), *Seismological Research Letters.*, 80, 784-798,
39 <https://doi.org/10.1785/gssrt.80.5.784>, 2009.

40 Dong, X.Z.: *Meso-Cenozoic structural features and evolution of Laoting depression and its surrounding*
41 *areas*, Beijing: China University of Geosciences (Beijing)., 2011.

1 Dreger, D., and Helmberger, D.: Source parameters of the Sierra Madre earthquake from regional and
2 local body waves, *Geophysical Research Letters.*, 18, 2015-2018,
3 <https://doi.org/10.1029/91GL02366>, 1991.

4 Du, H., Wang, J., Zhu Y.J., Wang, D.W., Xiao, F., and Xu, N.: Temporal and spatial variation
5 characteristics of b value of Tangshan M_s 5.1 earthquake in 2020, *North China Earthquake*
6 *Sciences.*, 39, 92-98, <https://doi.org/10.3969/j.issn.1003-1375.2021.03.014>, 2021.

7 Ellsworth, W.L.: Injection-induced earthquakes, *Science.*, 341, 1225942,
8 <https://doi.org/10.1126/science.1225942>, 2013.

9 Evans, K.F., Zappone, A., Kraft, T., Deichmann, N., and Moia, F.: A survey of the induced seismic
10 responses to fluid injection in geothermal and CO₂ reservoirs in Europe, *Geothermics.*, 41, 30-54,
11 <https://doi.org/10.1016/j.geothermics.2011.08.002>, 2012.

12 Fan, W.J., Cui, X.F., Hu, X.P., and Chen, J.W.: Focal mechanism solutions and spatio-temporal
13 variations of the present tectonic stress field in Capital Circle region, *Acta Seismologica Sinica.*,
14 41, 33-45, <https://doi.org/10.11939/jass.20180064>, 2019.

15 Feng, C.J., Qi, B.S., Wang, X.S., Zhang, P., Sun, M.Q., Meng, J., Tan, C.X., and Chen, Q.C.: Study of
16 fault activity risk in typical strong seismic regions in northern China by in-situ stress
17 measurements and the influence on the Xiong'an New Area, *Earth Science Frontiers.*, 26, 170-190,
18 <https://doi.org/10.13745/j.esf.sf.2019.4.17>, 2019.

19 Feng, C.J., Yang, Y.H., Ma, X.D., Qi, B.S., Zhang, P., Meng, J., Tan, C.X., and Chen, Q.C.: Local
20 stress perturbations associated with the 2008 Wenchuan M 8.0 earthquake near the Longmenshan
21 fault zone in the eastern margin of the Tibetan Plateau, *Journal of Asian Earth Sciences.*, 200,
22 104429, <https://doi.org/10.1016/j.jseaes.2020.104429>, 2020.

23 Feng, C.J., Zhang, P., Meng, J., Qi, B.S., Qin, X.H., Niu, L.L., Sun, D.S., Sun, W.F., Tan, C.X., and
24 Chen, Q.C.: In situ stress measurement at deep boreholes along the Tanlu fault zone and its
25 seismological and geological significance, *Progress in Geophysics.*, 32, 946-967,
26 <https://doi.org/10.6038/pg20170302>, 2017.

27 Ferris, J.G., Knowles, D.B., Brown, R.H., and Stallman, R.W. Theory of aquifer tests, *Geological*
28 *Survey Water-Supply Paper 1536-E.*, 1962.

29 Galis, M., Ampuero, J.P., Mai, P.M., and Cappa, F.: Induced seismicity provides insight into why
30 earthquake ruptures stop, *Science Advances.*, 3, 7528, <https://doi.org/10.1126/sciadv.app7528>,
31 2017.

32 Gao, K., and Harrison, P.J.: Generation of random stress tensors, *International Journal of Rock*
33 *Mechanics & Mining Sciences.*, 97, 18-26, <https://doi.org/10.1016/j.ijrmms.2016.12.011>, 2017.

34 Gao, Z.W., Xu, J., Song, C.Q., and Sun, J.B.: The segmental character of Zhangjiakou-Penglai fault,
35 *North China Earthquake Sciences.*, 19, 35-54, 2001.

36 Gaucher, E., Schoenball, M., Heidbach, O., Zang, A., Fokker, P., van Wees, J.D., and Kohl, T.:
37 Induced seismicity in geothermal reservoirs: a review of forecasting approaches, *Renewable and*
38 *Sustainable Energy Reviews.*, 52, 1473-1490, <http://dx.doi.org/10.1016/j.rser.2015.08.026>, 2015.

39 Gephart, J.W., and Forsyth, D.: An improved method for determining the regional stress tensor using
40 earthquake focal mechanism data: Application to the San Fernando earthquake sequence, *Journal*

1 of Geophysical Research Solid Earth., 89, 9305-9320, <https://doi.org/10.1029/JB089iB11p09305>,
2 1984.

3 Ghassemi, A., and Tao, Q.: Thermo-poroelastic effects on reservoir seismicity and permeability change,
4 Geothermics., 63, 210-224, <https://dx.doi.org/10.1016/j.geothermics.2016.02.006>, 2016.

5 Goebel, T.H.W., and Brodsky, E.E.: The spatial footprint of injection wells in a global compilation of
6 induced earthquake sequences, Science., 361, 899-904, <https://doi.org/10.1126/science.aat5449>,
7 2018.

8 Goebel, T.H.W., Weingarten, M., Chen, X., Haffener, J., and Brodsky, E.E.: The 2016 M_w 5.1 Fairview,
9 Oklahoma earthquakes: Evidence for long-range poroelastic triggering at >40 km from fluid
10 disposal wells, Earth and Planetary Science Letters., 472, 50-61,
11 <http://dx.doi.org/10.1016/j.epsl.2017.05.011>, 2017.

12 Grigoli, F., Cesca, S., Rinaldi, A.P., Manconi, A., López-Comino, J.A., Clinton, J.F., Westaway, R.,
13 Cauzzi, C., Dahm, T., and Wiemer, S.: The November 2017 M_w 5.5 Pohang earthquake: A possible
14 case of induced seismicity in South Korea, Science., 360, 1003-1006,
15 <https://doi.org/10.1126/science.aat2010>, 2018.

16 Guo, H., Jiang, W.L., and Xie, X.S.: Late-Quaternary strong earthquakes on the seismogenic fault of
17 the 1976 M_s 7.8 Tangshan earthquake, Hebei, as revealed by drilling and trenching, Sci China
18 Earth Sci., 41, 1009-1028, <https://doi.org/10.1007/s11430-011-4218-x>, 2011.

19 Guo, H., and Zhao, J.X.: The surface rupture zone and paleoseismic evidence on the seismogenic fault
20 of the 1976 M_s 7.8 Tangshan earthquake, China, Geomorphology., 327, 297-306,
21 <https://doi.org/10.1016/j.geomorph.2018.11.006>, 2019.

22 Guo, S.M., Li, Z.Y., Cheng, S.P., Chen, X.C., Chen, X.D., Yang, Z.E., and Li, R.C.: Discussion on the
23 regional structural background and the seismogenic model of the Tangshan earthquake, Scientia
24 Geologica Sinica., 4, 305-321, 1977.

25 Hao, S.J., Li, J.H., Yu, Z.S., and Chu, B.G.: Shallow seismic exploration of the seismogenic
26 structures of Tangshan earthquake, Earthquake Research in China., 14, 78-84, 1998.

27 Häring, M.O., Schanz, U., Ladner, F., and Dyer, B.C.: Characterisation of the Basel 1 enhanced
28 geothermal system, Geothermics, 37, 469-495, <https://doi.org/10.1016/j.geothermics.2008.06.002>,
29 2008.

30 Healy, J.H., Rubey, W.W., Griggs, D.T., and Raleigh, C.: The Denver earthquakes, Science., 161,
31 1301-1310, <https://doi.org/10.1126/science.161.3848.1301>, 1968.

32 Henderson, J.R., Barton, D.J., and Foulger, G.R.: Fractal clustering of induced seismicity in the
33 Geysers geothermal area, California, Geophysical Journal International., 139, 317-324.
34 <https://doi.org/10.1046/j.1365-246x.1999.00939.x>, 1999.

35 Hennings, P.H., Lund Snee, J.E., Osmond, J.L., DeShon, H.R., Dommissé, R., Horne, E., Lemons, C.,
36 and Zoback, M.D.: Injection-induced seismicity and fault-slip potential in the Fort Worth Basin,
37 Texas, Bulletin of the Seismological Society of America., 109, 1615-1634,
38 <https://doi.org/10.1785/0120190017>, 2019.

1 Hergert, T., and Heidbach, O.: Geomechanical model of the Marmara Sea region-II.3-D contemporary
2 background stress field, *Geophysical Journal International.*, 185, 1090-1102,
3 <https://doi.org/10.1111/j.1365-246x.2011.04992.x>, 2011.

4 Hickman, S., and Zoback, M.D.: Stress orientations and magnitudes in the SAFOD pilot hole,
5 *Geophysical Research Letters.*, 31, L15S12, <https://doi.org/10.1029/2004GL020043>, 2004.

6 Hsieh, P.A., and Bredehoeft, J.D.: A reservoir analysis of the Denver earthquakes: A case of induced
7 seismicity, *Journal of Geophysical Research.*, 86, 903-920.
8 <https://doi.org/10.1029/JB086iB02p00903>, 1981.

9 Huang, B.S., and Yeong, T.Y.: The fault ruptures of the 1976 Tangshan earthquake sequence inferred
10 from coseismic crustal deformation, *Bulletin of the seismological Society of America.*, 87,
11 1046-1057, <https://doi.org/10.1029/96JB03669>, 1997.

12 Huang, J.C., and Wan, Y.G.: Present tectonic stress field in the capital region of China determined
13 from small and strong earthquake focal mechanisms, *Earthquake.*, 35, 17-27, 2015.

14 Huang, L.Y., Yang, S.X., Cui, X.F., Chen, Q.C., and Yao, R.: Analysis of characteristics of measured
15 stress and stability of faults in North China, *Rock and Soil Mechanics.*, 34, 204-213, 2013.

16 Hubbert, M.K., and Rubey, W.W.: Role of fluid pressure in mechanics of overthrust faulting:
17 1.Mechanics of fluid-filled porous solids and its application to overthrust faulting, *Geological*
18 *Society of America Bulletin.*, 70, 115-166,
19 [https://doi.org/10.1130/0016-7606\(1959\)70\[115:ROFPIM\]2.0.CO;2](https://doi.org/10.1130/0016-7606(1959)70[115:ROFPIM]2.0.CO;2), 1959.

20 Hunt, .TM., and Latter, J.H.: A survey of seismic activity near Wairakei geothermal field, New Zealand,
21 *Journal of Volcanology and Geothermal Research.*, 14, 319-334,
22 [https://doi.org/10.1016/0377-0273\(82\)90068-3](https://doi.org/10.1016/0377-0273(82)90068-3), 1982.

23 Jaeger, J.C., Cook, N.G.W., and Zimmerman, R.W.: *Fundamentals of Rock Mechanics*, 4th Edition,
24 Wiley-Blackwell., 2007.

25 Jiang, W.L.: Discussion on seismogenic fault of the 1976 Tangshan earthquake, *Seismology and*
26 *Geology.*, 28, 312-318, 2006.

27 Keranen, K.M., Weingarten, M.W., Abers, G.A., Bekins, B.A., and Ge, S.: Sharp increase in central
28 Oklahoma seismicity since 2008 induced by massive wastewater injection, *Science.*, 345, 448-451,
29 <https://doi.org/10.1126/science.1255802>, 2014.

30 Kim, K.H., Ree, J.H., Kim, Y.H., Kim, S.S., Kang, S.Y., and Seo, W.: Assessing whether the 2017
31 M_w 5.4 Pohang earthquake in South Korea was an induced event, *Science.*, 360, 1007-1009,
32 <https://doi.org/10.1126/science.aat6081>, 2018.

33 Kim, W.Y.: Induced seismicity associated with fluid injection into a deep well in Youngstown, Ohio,
34 *Journal of Geophysical Research: Solid Earth.*, 118, 3506-3518,
35 <https://doi.org/10.1002/jgrb.50247>, 2013.

36 Langenbruch, C., and Shapiro, S.A.: Quantitative analysis of rock stress heterogeneity: Implications for
37 the seismogenesis of fluid-injection-induced seismicity, *Geophysics.*, 80, WC730-WC88,
38 <https://doi.org/10.1190/geo2015-0061.1>, 2015.

- 1 Lee, H., and Ong, S.H.: Estimation of in situ stresses with Hydro-fracturing tests and a statistical
2 method, *Rock Mechanics and Rock Engineering.*, 51, 779-799,
3 <https://doi.org/10.1007/s00603-017-1349-1>, 2018.
- 4 Lee, K.K., Ellsworth, W.L., Giardini, D., Townend, J., Ge, S.M., Toshihiko, S., Yeo, I.W., Kang, T.S.,
5 Junkee, R., Sheen, D.H., Chang, C.D., Woo, J.U., and Langenbruch, C.: Managing
6 injection-induced seismic risks, *Science.*, 364, 730-732, <https://doi.org/10.1126/science.aax1878>,
7 2019.
- 8 Lei, X.L., Huang, D.J., Su, J.R., Jiang, G.M., Wang, X.L., Wang, H., Guo, X., and Fu, H.: Fault
9 reactivation and earthquakes with magnitudes of up to $M_w4.7$ induced by shale-gas hydraulic
10 fracturing in Sichuan Basin, China, *Scientific Reports.*, 7, 1-12,
11 <https://doi.org/10.1038/s41598-017-08557-y>, 2017.
- 12 Li, J.H., Hao, S.J., Hu, Y.T., Yu, Z.S., and Chu, B.G.: A study on activity of the seismogenic fault for
13 the Tangshan earthquake of 1976, *Seismology and Geology.*, 20, 27-33, 1998.
- 14 Li, P., Cai, M.F., Miao, S.J., and Guo, Q.F.: New insights into the current stress field around the Yishu
15 fault zone, eastern China, *Rock Mechanics and Rock Engineering.*, 52, 4133-4145,
16 <https://doi.org/10.1007/s00603-019-01792-x>, 2019.
- 17 Li, Q.Z., Zhang, Z.L., Jin, Y.M., Yu, X.C., and Li, Z.Y.: Focal mechanisms of Tangshan earthquakes,
18 *Seismology and Geology.*, 2, 59-67, 1980.
- 19 Li, Y.L., and Dong, Y.X.: Influence of reserved stope roof thickness on its stability in the Macheng
20 iron mine, *Hydrogeology & Engineering Geology.*, 40, 79-82, <https://doi.org/10.16030/j.cnki.issn.1000-3665.2013.02.017>, 2013.
- 22 Li, S.X., Liu, B.H., Hua, Q.F., Zhao, Y.X., and Liu, C.G.: Characters of the Zhangjiakou-Penglai fault
23 zone activity in the Bohai Sea since late Quaternary, *Advance in Marine Science.*, 27, 332-341,
24 [https://doi.org/10.1016/S1874-8651\(10\)60080-4](https://doi.org/10.1016/S1874-8651(10)60080-4), 2009.
- 25 Li, W.J., Wang, P.D., and Chen, Q.F.: Moment tensor inversion of focal mechanism for the aftershock
26 sequence of 1982 Lulong M_s 6.1 earthquake, *Acta Seismologica Sinica.*, 19, 115-122.
27 <https://doi.org/10.1007/s11589-002-0115-x>, 2006.
- 28 Li, Z.W., Ni, S.D., Roecker, S., Bao, F., Wei, X., and Yuen, D.A.: Seismic imaging of source region in
29 the 1976 $M_s7.8$ Tangshan earthquake sequence and its implications for the seismogenesis of
30 intraplate earthquakes. *Bulletin of the Seismological Society of America.*, 108, 1302-1313,
31 <https://doi.org/10.1785/0120170389>, 2018.
- 32 Lin, X.D., Yuan, H.Y., Xu, P., Yang, X., Xu, Z.G., Sun, H.X., Hou, L.J., Xu, S.T., and Xi, C.X.:
33 Zonational characteristics of earthquake focal mechanism solutions in North China, *Chinese
34 Journal of Geophysics.*, 60, 4589-4622, <https://doi.org/10.6038/cjg20171206>, 2017.
- 35 Liu, B.J., Qu, G.S., Sun, M.X., Liu, K., Zhao, C.B., Xu, X.W., Feng, S.Y., and Kou, K.P.: Crustal
36 structures and tectonics of Tangshan earthquake area: results from deep seismic reflection
37 profiling, *Seismology and Geology.*, 33, 901-912,
38 <https://doi.org/10.3969/j.issn.0253-4967.2011.04.014>, 2011.
- 39 Liu, H.Y., Chen, Y.K., Yan, C.G., and Fei, Y.: Seismic risk evaluation on blind faults in Tianjin
40 offshore areas, *Technology for Earthquake Disaster Prevention.*, 8, 146-155, 2013.

- 1 Lund Snee, J.E., and Zoback, M.D.: State of stress in Texas: Implications for induced seismicity,
2 Geophysical Research Letters., 43, 1-7, <https://doi.org/10.1002/2016GL070974>, 2016.
- 3 Lund Snee, J.E., and Zoback, M.D.: State of stress in the Permian Basin, Texas and New Mexico:
4 Implications for induced seismicity, The Leading Edge., 37, 127-134,
5 <https://doi.org/10.1190/tle37020127.1>, 2018.
- 6 McGarr, A.: Maximum magnitude earthquakes induced by fluid injection, Journal of Geophysical
7 Research: Solid Earth., 119, 1008-1019, <https://doi.org/10.1002/2013JB010597>, 2014.
- 8 McGarr, A., Bekins, B., Burkardt, N., Dewey, J., Earle, P., Ellsworth, W.L., Ge, S., Hickman, S.,
9 Holland, A., Majer, E., Rubinstein, J., and Sheehan, A.: Coping with earthquakes induced by fluid
10 injection, Science., 347, 830-831, <https://doi.org/10.1126/science.aaa0494>, 2015.
- 11 McTigue, D.F.: Flow to a heated borehole in porous, thermoelastic rock: Analysis, Water Resources
12 Research., 26, 1763-1774, [https://doi.org/10.1016/0148-9062\(91\)92334-U](https://doi.org/10.1016/0148-9062(91)92334-U), 1990.
- 13 Michael, A.J.: Use of focal mechanisms to determine stress: a control study, Journal of Geophysical
14 Research Solid Earth., 92, 357-368, <https://doi.org/10.1029/JB092iB01p00357>, 1984.
- 15 Minson, S.E., and Dreger, D.S.: Stable inversions for complete moment tensors, Geophysical Journal
16 International., 174, 585-592, <https://doi.org/10.1111/j.1365-246X.2008.03797.x>, 2008.
- 17 Moeck, I., Kwiatek, G., and Zimmermann, G.: Slip tendency analysis, fault reactivation potential and
18 induced seismicity in a deep geothermal reservoir, Journal of structural Geology., 31, 1174-1182,
19 <https://doi.org/10.1016/j.jsg.2009.06.012>, 2009.
- 20 Murphy, H., Brown, D., Jung, R., Matsunaga, I., and Parker, R.: Hydraulics and well testing of
21 engineered geothermal reservoirs, Geothermics., 28, 491-506.
22 <https://doi.org/10.2174/157019308786242197>, 1999.
- 23 Nábělek, J., Chen, W.P., and Ye, H.: The Tangshan earthquake sequence and its implications for the
24 evolution of the North China Basin, Journal of Geophysical Research., 92, 12615-12628,
25 <https://doi.org/10.1029/JB092iB12p12615>, 1987.
- 26 Nagano, K., Moriya, H., Asanuma, H., Sato, M., Niitsuma, and H., Kaieda, H.: Down-hole acoustic
27 emission measurement of hydraulic fracturing in Ogachi HDR model field, Journal of the
28 Geothermal Research Society of Japan., 16, 85-108, <https://doi.org/10.11367/grsj1979.16.85>,
29 1994.
- 30 Niu, L.L., Du, J.J., Feng, C.J., Meng, W., Li, G.Q., and Chen, Q.C: In-situ stress measurement of deep
31 borehole in east of Hebei and its significance, Acta Seismologica Sinica., 37, 89-102,
32 <https://doi.org/10.11939/jass.2015.01.008>, 2015.
- 33 Papadopoulos, I.S.: Nonsteady flow to a well in an infinite anisotropic aquifer, International association
34 of hydrology roches fissures proceedings dubrovnik symposium., 1, 21-31, 1965.
- 35 Peng, Y.Q., and Meng, L.P.: Seismic structures of Hebei province, China, The Hebei people's
36 Publishing House., 2017.
- 37 Qi, X.F., Shangguan, S.T., Zhang, G.B., Pan, M.M., Su, Y., Tian, L.L., Li, X., and Zhang, J.Y.: Site
38 selection and developmental prospect of a hot dry rock resource project in the Matouying Uplift,
39 Hebei Province, Earth Science Frontiers., 27, 094-102, <https://doi.org/10.13745/j.esf.2020.1.11>,
40 2020.

- 1 Qin, X.H., Chen, Q.C., Wu, M.L., Tan, C.X., Feng, C.J., and Meng, W.: In-situ stress measurements
2 along the Beichuan-Yingxiu fault after the Wenchuan earthquake, *Engineering Geology.*, 194,
3 114-122, <https://doi.org/10.1016/j.enggeo.2015.04.029>, 2015
- 4 Qin, X.H., Zhang, P., Feng, C.J., Sun, W.F., Tan, C.X., Chen, Q.C., and Peng, Y.R.: In situ stress
5 measurements and slip stability of major faults in Beijing region, China, *Chinese Journal of*
6 *Geophysics.*, 57, 2165-2180, <https://doi.org/10.1002/cjg2.20113>, 2014.
- 7 Qiu, Z.H., Ma, J., and Liu, G.X.: Discovery of the great fault of the Tangshan earthquake, *Seismology*
8 *and Geology.*, 27, 669-677, 2005.
- 9 Raleigh, C.B., Healy, J.H., and Bredehoeft, J.D.: An experiment in earthquake control at Rangely,
10 Colorado, *Science.*, 191, 1230-1237,
11 <https://doi.org/10.1126/science.191.4233.1230> PMID:17737698, 1976.
- 12 Ran, Z.J., Yang, Q.Y., Lv, G.J., Luo, Y.X., and Peng, Y.Q.: The preliminary study of the faults nearby
13 Luanxian County, North China *Earthquake Sciences.*, 31, 8-12,
14 <https://doi.org/10.3969/j.issn.1003-1375.2013.02.002>, 2013.
- 15 Rutledge, J.T., Phillips, W.S., and Mayerhofer, M.J.: Faulting induced by forced fluid injection and
16 fluid flow forced by faulting: An interpretation of hydraulic-fracture microseismicity, Carthage
17 Cotton Valley Gas field, Texas, *Bulletin of Seismological Society of America.*, 94, 1817-1830,
18 <https://doi.org/10.1785/012003257>, 2004.
- 19 Sanyal, S.K., and Butler, S.J.: An analysis of power generation prospects from enhanced geothermal
20 systems, In: *Proceedings World Geothermal Congress 2005, Antalya, Turkey.*, 24-29, 2005.
- 21 Segall, P., and Fitzgerald, S.D.: A note on induced stress changes in hydrocarbon and geothermal
22 reservoirs, *Tectonophysics.*, 289, 117-128, [https://doi.org/10.1016/S0040-1951\(97\)00311-9](https://doi.org/10.1016/S0040-1951(97)00311-9), 1998.
- 23 Shapiro, S.A., C. Dinske., and C. Langenbruch.: Seismogenic index and magnitude probability of
24 earthquakes induced during reservoir fluid stimulations, *The Leading Edge.*, 29, 304-309,
25 <https://doi.org/10.1190/1.3353727>, 2010.
- 26 Shapiro, S.A., Rentsch, S., and Rothert, E.: Characterization of hydraulic properties of rocks using
27 probability of fluid-induced microearthquakes, *Geophysics.*, 70, F27-F33,
28 <https://doi.org/10.1190/1.1897030>, 2005.
- 29 Shedlock, K.M., Baranowski, J., Xiao, W., and Hu, X.L.: The Tangshan aftershock sequence, *Journal*
30 *of Geophysical Research.*, 92, 2791-2803, <https://doi.org/10.1029/JB092iB03p02791>, 1987.
- 31 Simiyu, S.M.: Induced micro-seismicity during well discharge, *Geothermics.*, 28, 785-802,
32 [https://doi.org/10.1016/S0375-6505\(99\)00043-7](https://doi.org/10.1016/S0375-6505(99)00043-7), 1999.
- 33 Simpson, R.W.: Quantifying Anderson's fault types, *Journal of Geophysical Research Solid Earth.*, 102,
34 17909-17919, <https://doi.org/10.1029/97JB01274>, 1997.
- 35 Snoke, J.A.: Traveltime tables for iasp91 and ak135, *Seismological Research Letter.*, 80, 260-262,
36 <https://doi.org/10.1785/gssrl.80.2.260>, 2009.
- 37 Tan, C.X., Hu, Q.Y., Zhang, P., Feng, C.J., and Qin, X.H.: Present tectonic stress adjustment process
38 before and after Japan M_w 9.0 earthquake in North and Northeast China and its research
39 significance, *Earth Science Frontiers.*, 22, 345-359, <https://doi.org/10.13745/j.esf.2015.01.030>,
40 2015.

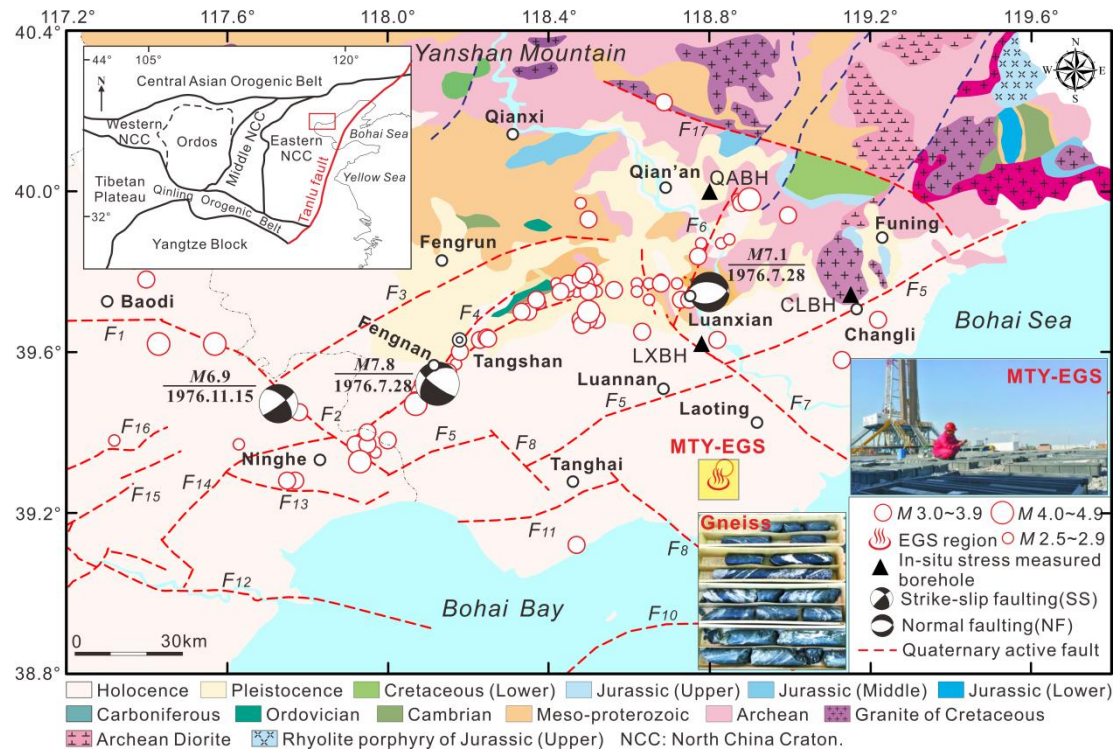
- 1 Tan, C.X., Zhang, P., Feng, C.J., Qin, X.H., Sun, W.F., Chen, Q.C., and Wu, M.L.: An approach to
2 deep borehole crustal stress measuring and real-time monitoring and its application in
3 seismogeology research in Capital Beijing region, *Acta Geologica Sinica.*, 88, 1436-1452, 2014.
- 4 Terakawa, T., Miller, S.A., and Deichmann, N.: High fluid pressure and triggered earthquakes in the
5 enhanced geothermal system in Basel, Switzerland, *Journal of Geophysical Research.*, 117, 1-15,
6 <https://doi.org/10.1029/2011JB008980>, 2012.
- 7 Tharaka, D.R., Wu, W., Ji, Y.L., and Ranjith, P.G.: Understanding injection-induced seismicity in
8 enhanced geothermal systems: From the coupled thermo-hydro-mechanical-chemical process to
9 anthropogenic earthquakes prediction, *Earth-Science Reviews.*, 205, 103182.
10 <https://doi.org/10.1016/j.earscirev.2020.103182>, 2020.
- 11 Townend, J., and Zoback, M.D.: How faulting keeps the crust strong, *Geology.*, 28, 399-402,
12 [https://doi.org/10.1130/0091-7613\(2000\)28<399:HFKTCS>2.0.CO;2](https://doi.org/10.1130/0091-7613(2000)28<399:HFKTCS>2.0.CO;2), 2000.
- 13 Van der Elst, N. J., M. T. Page., D. A. Weiser., T. H. W. Goebel., and S. M. Hosseini.: Induced
14 earthquake magnitudes are as large as (statistically) expected, *Journal of Geophysical Research:*
15 *Solid Earth.*, 121, 4575-4590, <https://doi.org/10.1002/2016JB012818>, 2016.
- 16 Vavryčuk, V.: Iterative joint inversion for stress and fault orientations from focal mechanisms,
17 *Geophysical Journal International.*, 199, 69-77, <https://doi.org/10.1093/gji/ggu224>, 2014.
- 18 Verberne, B.A., and He, .CR., and Christopher, J.S.: Frictional properties of sedimentary rocks and
19 natural fault gouge from the Longmenshan fault zone, Sichuan, China, *Bulletin of the*
20 *Seismological Society of America.*, 100, 2767-2790, <https://doi.org/10.1785/0120090287>, 2010.
- 21 Walsh, F.R., and Zoback, M.D.: Oklahoma's recent earthquakes and saltwater disposal, *Science*
22 *Advances.*, 1, e1500195, <https://doi.org/10.1126/sciadv.1500195>, 2015
- 23 Walsh, F.R., and Zoback, M.D.: Probabilistic assessment of potential fault slip related to
24 injection-induced earthquakes: Application to north-central Oklahoma, USA, *Geology.*, 44,
25 G38275.1, <https://doi.org/10.1130/G38275.1>, 2016.
- 26 Walsh III, R., Zoback, M.D., Pais, D., Weingarten, M., and Tyrrell, T.: FSP1.0: A program for
27 probabilistic estimation of fault slip potential resulting from fluid injection, Free at
28 [SCITS.stanford.edu/software.](https://SCITS.stanford.edu/software/), 2017.
- 29 Walters, R.J., Zoback, M.D., Baker, J.W., and Beroza, G.C.: Characterizing and responding to seismic
30 risk associated with earthquake potentially triggered by fluid disposal and hydraulic fracturing,
31 *Seismological Research Letters.*, 86, 1110-1118, <https://doi.org/10.1785/0220150048>, 2015.
- 32 Wan, Y.G., Shen, Z.K., Diao, G.L., Wang, F.J., Hu, X.L., and Shen, S.Z.: An algorithm of fault
33 parameter determination using distribution of small earthquakes and parameters of regional stress
34 field and its application to Tangshan earthquake sequence, *Chinese Journal of Geophysics.*, 51,
35 793-804, 2008.
- 36 Wan, Y.G., Wan, Y.K., Jin, Z.T., Sheng, S.Z., Liu, Z.C., Yang, F., and Feng, T.: Rupture distribution
37 of the 1976 Tangshan earthquake sequence inverted from geodetic data, *Chinese Journal of*
38 *Geophysics.*, 60, 3378-3395, <https://doi.org/10.1002/cjg2.30070>, 2017.
- 39 Wang, J.H., Zhang, Y., and Wang, Y.J.: Analysis of influencing mining factors through 3D geological
40 modeling Macheng mining area., *China Mining Magazine.*, 22, 127-134, 2013.

- 1 Wei, S., Avouac, J.P., Hudnut, K.W., Donnellan, A., Parker, J.W., Graves, R.W., Helmberger, D.,
2 Fielding, E., Liu, Z., Cappa, F., and Eneva, M.: The 2012 Brawley swarm triggered by
3 injection-induced aseismic slip, *Earth and Planetary Science Letters.*, 422, 115-125,
4 <https://doi.org/10.1016/j.epsl.2015.03.054>, 2015.
- 5 Weingarten, M., Ge, S., Godt, J.W., Bekins, B.A., and Rubinstein, J.L.: High-rate injection is
6 associated with the increase in U.S. mid-continent seismicity, *Science.*, 348, 1336-1340.
7 <https://doi.org/10.1126/science.aab1345>, 2015.
- 8 Woo, J.U., Kim, M., Sheen, D.H., Kang, T.S., Rhie, J., Grigoli, F., Ellsworth, W.L., and Giardini, D.:
9 An in-depth seismological analysis revealing a causal link between the 2017 M_w 5.5 Pohang
10 earthquake and EGS project, *Journal of Geophysical Research: Solid Earth.*, 124, 1-19,
11 <https://doi.org/10.1029/2019JB018368>, 2019.
- 12 Xiao, W.W., Huang, Q., and Wang, R.J.: Distribution and fractal characteristics of stress drop in
13 different earthquake regions, *Acta Seismologica Sinica.*, 14, 281-288, 1992.
- 14 Xu, J.R., Zhao, Z.X., and Ishikawa, Yuzo.: Regional characteristics of crustal stress field and tectonic
15 motions in and around Chinese mainland, *Chinese Journal of Geophysics.*, 51, 770-781,
16 <https://doi.org/10.1016/j.chemgeo.2008.02.011>, 2008.
- 17 Yan, C.G., Wang, Z.S., Chen, Y.K., Ren, F., and Gao, W.P.: Comprehensive survey and investigation
18 on the exact spatial location and activity of the Hangu fault in Tianjin, *Earthquake Research in
19 China.*, 30, 501-513, 2014.
- 20 Yang, K.S., Hu, P., and Dang, X.C.: A discussion on the generating mechanism of 1976 Tangshan
21 earthquake based on the geologic structure of northern Huabei Basin, *Earth Science Frontiers.*, 17,
22 263-270., <https://doi.org/10.1017/S0004972710001772>, 2010.
- 23 Yang, S.X., Yao, R., Cui, X.F., Chen, Q.C., and Huang, L.Y.: Analysis of the characteristics of
24 measured stress in Chinese mainland and its active blocks and North-South seismic belt, *Chinese
25 Journal of Geophysics.*, 55, 4207-4217, <https://doi.org/10.6038/j.issn.0001-5733.2012.12.032>,
26 2012.
- 27 Yang, Y.Q., Wang, X.S., Wan, Y.G., Sheng, S.Z., and Chen, T.: Seismogenic fault segmentation of
28 Tangshan earthquake sequence derived from focal mechanism solutions, *Acta Seismologica
29 Sinica.*, 38, 632-643, <https://doi.org/10.11939/jass.2016.04.009>, 2016.
- 30 Ye, H., Shedlock, K.M., Hellinger, S.J., and Slater, J.G.: The north china basin: An example of a
31 Cenozoic rifted intraplate basin, *Tectonics.*, 4, 153-169, <https://doi.org/10.1029/TC004i002p00153>,
32 1985.
- 33 You, H.C., Xu, X.W., Wu, J.P., and He, Z.Q.: Study on the relationship between shallow and deep
34 structures in the 1976 Tangshan earthquake area, *Seismology and Geology.*, 24, 571-582, 2002.
- 35 Yue, G.F., Deng, X.F., Xing, L.X., Lin, W.J., Liu, F., Liu, Y.G., and Wang, G.L.: Numerical
36 simulation of hot dry rock exploitation using enhanced geothermal systems in Gonghe Basin.
37 *Science & Technology Review.*, 33, 62-67, <https://doi.org/10.3981/j.issn.1000-7857.2015.19.010>,
38 2015.

- 1 Zang, A., Oye, V., Jousset, P., Deichmann, N., Gritto, R., McGarr, A., Majer, E., and Bruhn, D.:
2 Analysis of induced seismicity in geothermal reservoirs-An overview, *Geothermics.*, 52, 6-21.
3 <https://doi.org/10.1016/j.geothermics.2014.06.005>, 2014.
- 4 Zeng, Y.C., Su, Z., and Wu, N.Y.: Numerical simulation of heat production potential from hot dry rock
5 by water circulating through two horizontal wells at Desert Peak geothermal field, *Energy.*, 56,
6 92-107, <http://dx.doi.org/10.1016/j.energy.2013.04.055>, 2013.
- 7 Zhang, B.J., Gao, J., Li, Y.Y., Wang, G.L., Li, J., Xing, Y.F., and Zhao, T.: Genetic mechanism and
8 indicative significance of hot dry rock in the Matouying, Hebei province, *Acta Geologica Sinica.*,
9 94, 2036-2051, <https://doi:10.19762/j.cnki.dizhixuebao.2020226>, 2020.
- 10 Zhang, H.Z., Diao, G.L., Chen, Q.F., Hu, X.L., Wang, X.S., and Zhang, Y.G.: Focal mechanism
11 analysis of the recent earthquakes in Tangshan seismic region of M 7.6 in 1976, *Journal of*
12 *Seismological Research.*, 31, 1-6, 2008.
- 13 Zhang, L.L., Song, F., Liu, X.S., She, S.Q., and Liu, D.J.: Research on the influence of Jidong iron
14 exploitation on regional groundwater environment, *Ground water.*, 36, 91-94, 2014.
- 15 Zhang, S.H., and Ma, X.D.: Global frictional equilibrium via stochastic, local Coulomb frictional slips,
16 *Journal of Geophysical Research: Solid Earth.*, 126, e2020JB021404,
17 <https://doi.org/10.1029/2020JB021404>, 2021.
- 18 Zhang, S.X., Wang, X.S., Chen, T., Gong, M., and Shan, L.J.: Seismic space-time evolution
19 characteristics in Tangshan old seismic region during the past 40 years, *North China Earthquake*
20 *Sciences.*, 35, 32-37, <https://doi.org/10.3969/j.issn.1003-1375-2017.01.005>, 2017.
- 21 Zhang, W., Zhang, Q., Liu, Y.H., Zhu, W.P., and Tong, J.: Characteristics of magnetic and gravity
22 anomalies of Lengkou fault in eastern Hebei and its geological functions, *Geophysical &*
23 *Geochemical Exploration.*, 37, 769-774, <https://doi.org/10.11720/j.issn.1000-8918.2013.5.02>,
24 2013.
- 25 Zhang, Y., Gao, L., Liu X.C., Zhao, Y., Wang, D., and Zhang, J.Y.: Drilling technology of the M-1
26 well in hot dry rock of Matouying, Tangshan, *Geology and Exploration.*, 58, 176-186, 2022.
- 27 Zhao, G.M., and Yang, G.S.: Focal stress field by water injection-induced earthquakes and
28 characteristics of coda wave attenuation, *Seismology and Geology.*, 12, 303-310, 1990.
- 29 Zhao, Y.X.: The analysis of hydrocarbon accumulation conditions of the buried hill in
30 Matouying-uplift-belt in Huanghua depression, Beijing: China University of Geosciences
31 (Beijing)., 2014.
- 32 Zheng, B.H., Guo, S.M., and Xu, H.M.: Preliminary study of principal features of the NW and NWW
33 trending fault structures in the Yanshan region, *Seismology and Geology.*, 3, 31-40, 1981.
- 34 Zheng, Y.P., Wang, Y., Chen, Y.K., and Han, G.Z.: Shallow tectonic characteristics of the Haihe fault
35 in Tanggu area, Tianjin municipality, *Advances in Marine Science.*, 24, 307-313,
36 [https://doi.org/10.1016/S1001-8042\(06\)60021-3](https://doi.org/10.1016/S1001-8042(06)60021-3), 2006.
- 37 Zhou, C.C.: Studies on the structure mode of Baigezhuang region and the identification and prediction
38 of structure fracture of reservoirs, Guangzhou: Guangzhou Institute of Geochemistry, Chinese
39 Academy of Sciences., 2003.

1 Zhu, S.Y., Feng, C.J., Xing, L.X., Ren, Y.Z., Qi, B.S., Zhang, P., and Tan, C.X.: Changes in fault slip
 2 potential due to water injection in the Rongcheng deep geothermal reservoir, Xiong'an New Area,
 3 North China, *Water.*, 14, 410, <https://doi.org/10.3390/w14030410>.
 4 Zoback, M.D., Barton, C.A., Brudy, M., Castillo, D.A., Finkbeiner, T., Grollmund, B.R., Moos, D.B.,
 5 Peska, P., Ward, C.D., and Wiprut, D.J.: Determination of stress orientation and magnitude in
 6 deep wells, *International Journal of Rock Mechanics & Mining Sciences.*, 40, 1049-1076,
 7 <https://doi.org/10.1016/j.ijrmms.2003.07.001>, 2003.
 8 Zoback, M.D., and Gorelick, S.M.: Earthquake triggering and large-scale geologic storage of carbon
 9 dioxide, *Proceedings of the National Academy of Sciences of the United States of America*, 109,
 10 10164-10168, <https://doi.org/10.1073/pnas.1202473109>, 2012.
 11 Zoback, M.D., and Healy, J.H.: In situ stress measurements to 3.5 km depth in the Cajon Pass
 12 Scientific Research Borehole: Implications for the mechanics of crustal faulting, *Journal of*
 13 *Geophysical Research.*, 97, 5039-5057, <https://doi.org/10.1029/91JB02175>, 1992.
 14 Zoback, M.L.: First- and second- order patterns of stress in the lithosphere: The World Stress Map
 15 Project, *Journal of Geophysical Research Solid Earth.*, 98, 11703-11728,
 16 <https://doi.org/10.1029/92JB00132>, 1992.

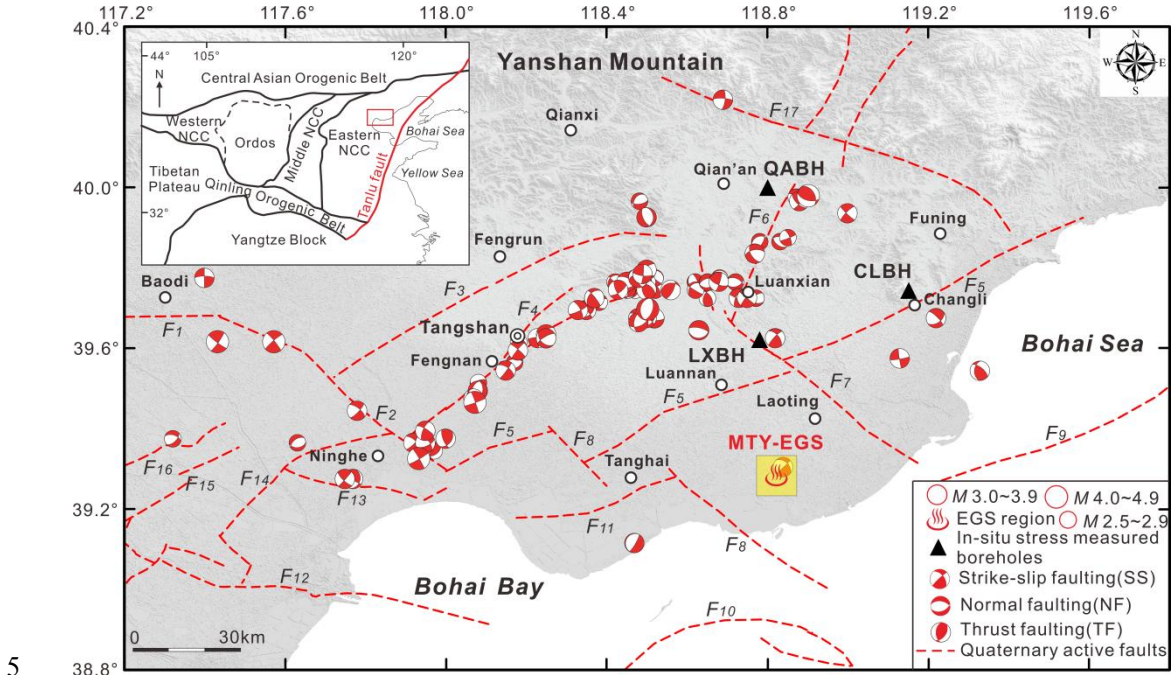
17
 18



19 **Figure 1.** The geological-seismogenic structures and the earthquakes ($M \geq 2.5$) from 2006 to 2019 in the Tangshan
 20 seismic region, North China (modified after Feng et al. (2019)). The earthquakes are gathered from the National
 21 Earthquake Data Center (NEDC), China (<https://data.earthquake.cn>). Focal mechanisms of the Tangshan M 7.8
 22 (7.28/1976), Luanxian M 7.1 (7.28/1976), and Ninghe M 6.9 (11.15/1976) earthquakes were determined by Huang
 23 and Yeong (1997). The tectonic faults in the Tangshan seismic region are as follows (Guo et al. 2011): F_1 -Baodi
 24 fault; F_2 -Jiyunhe fault; F_3 -Yejituo fault; F_4 -Tangshan fault belt; F_5 -Changli-Ninghe fault; F_6 -Lulong fault;
 25 F_7 -Luanxian-Laoting fault; F_8 -Baigezhaung fault; F_9 -Qinbei fault; F_{11} -Xi'nanzhuang fault; F_{12} -Haihe fault;
 26

1 F_{13} -Hangu fault; F_{14} -Cangdong fault; F_{17} -Lengkou fault. The yellow square denotes the Matouying (MTY) enhanced geothermal system (EGS) field being approximately 90 km away from the Tangshan City in Hebei province, China (Qi et al., 2020; Zhang et al., 2020).

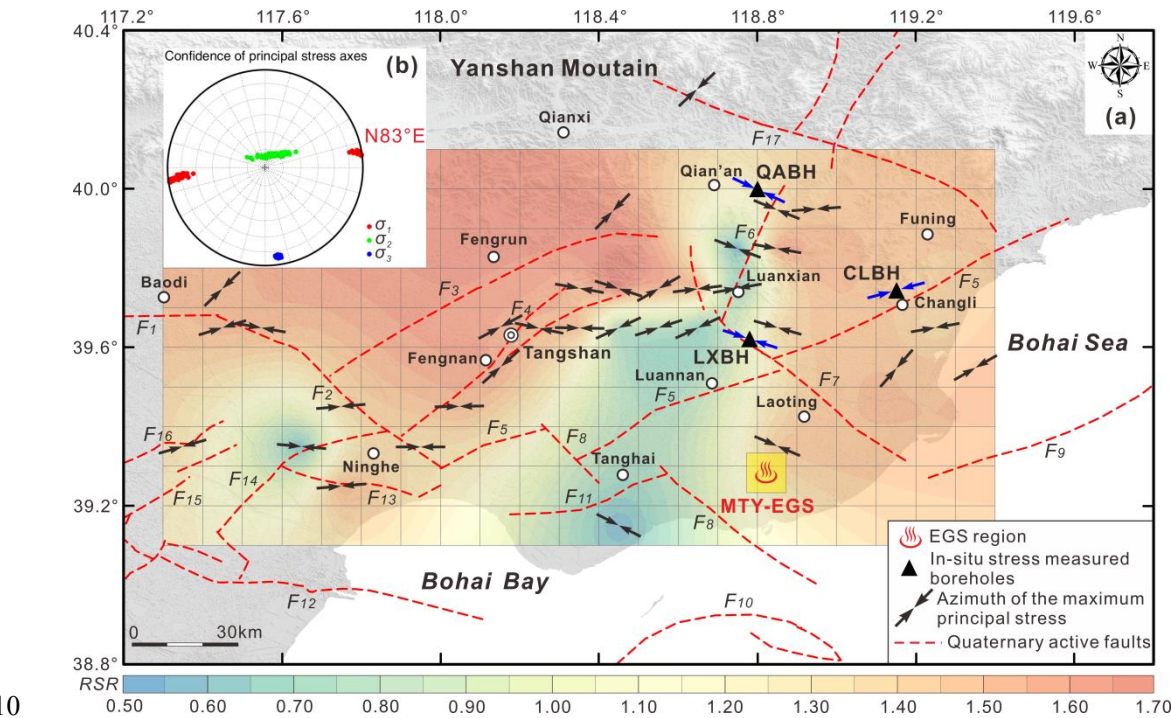
2



3

4
5
6 **Figure 2.** Focal mechanisms from 98 earthquakes ($M \geq 2.5$) from 2006 to 2019 in the Tangshan seismic region
7 (gathered from Lin et al. (2017)) and in situ stress measured boreholes (black triangle) by hydraulic fracturing
8 method on the north of the MTY EGS field (Tan et al., 2014; Niu et al., 2015; Feng et al., 2019).

9

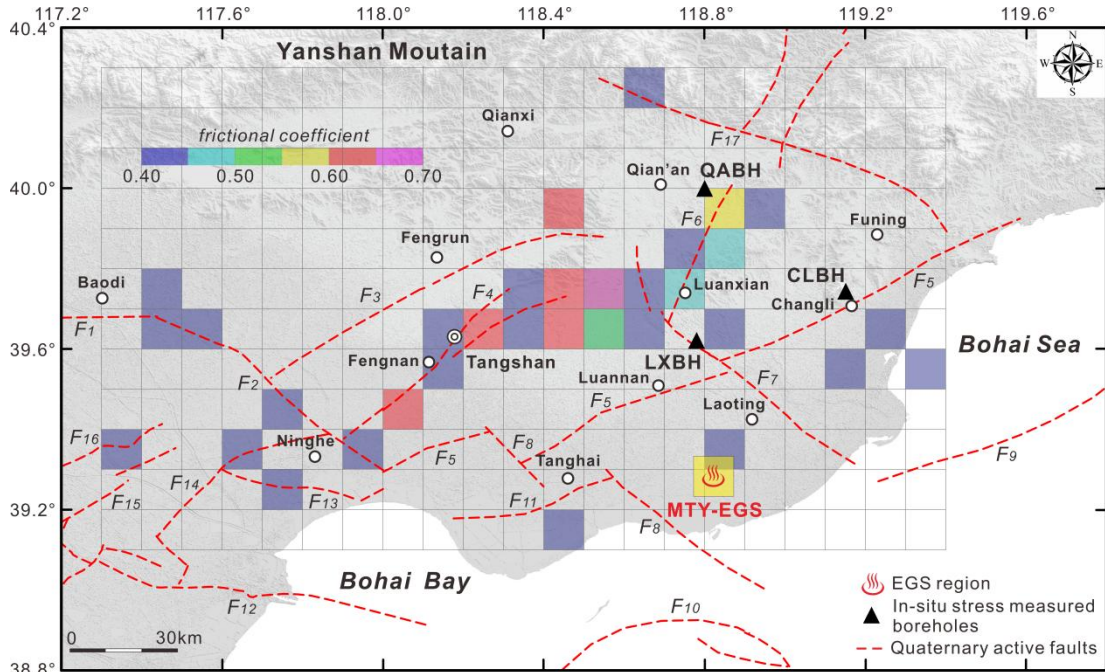


10

11 **Figure 3.** Crustal stress field in the Tangshan seismic region, as determined by inversion of 98 focal mechanisms
12 shown in Fig.2 using STRESSINVERSE software package (Vavryčuk, 2014). (a) The results of the inversion
13 in each bin ($0.1^\circ \times 0.1^\circ$) include the predominant maximum principal compressive stress orientation (σ_1) and the

1 regime stress ratio (*RSR*). **(b)** The dominant σ_1 orientation in the Tangshan seismic region was constrained using all
 2 98 focal mechanisms with a confidence interval of 95%.

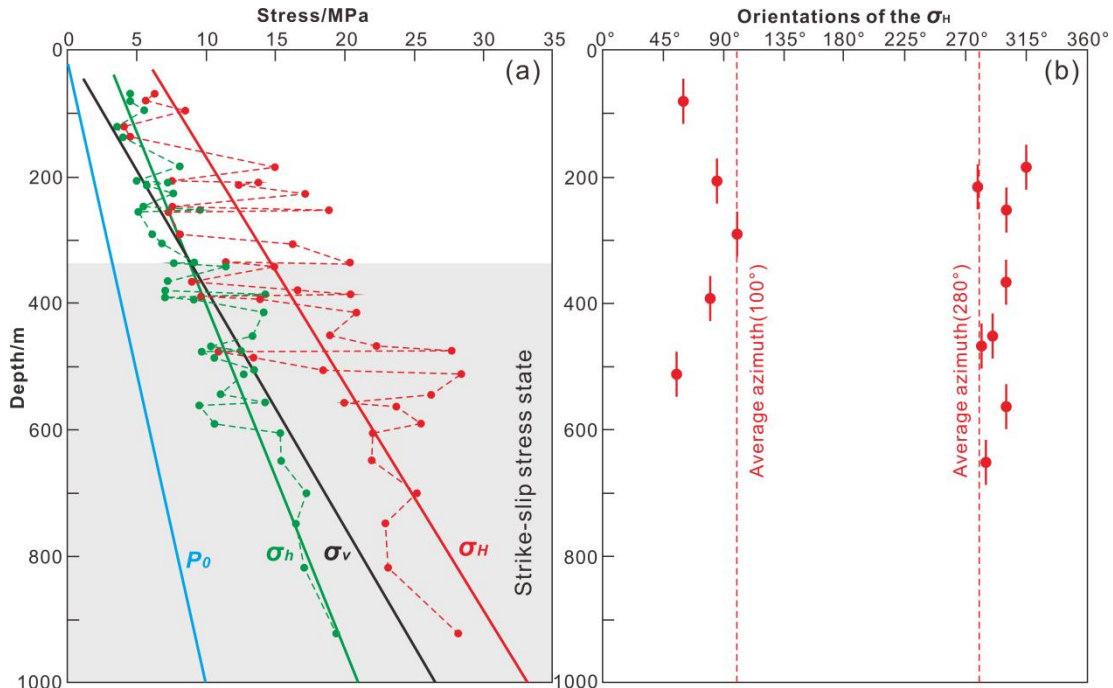
3



4

5 **Figure 4.** The critical coefficient of friction of the main seismic faults in the Tangshan seismic region, as
 6 determined by inversion of 98 focal mechanisms (seen in Figure 2) using STRESSINVERSE software package
 7 (Vavryčuk, 2014).

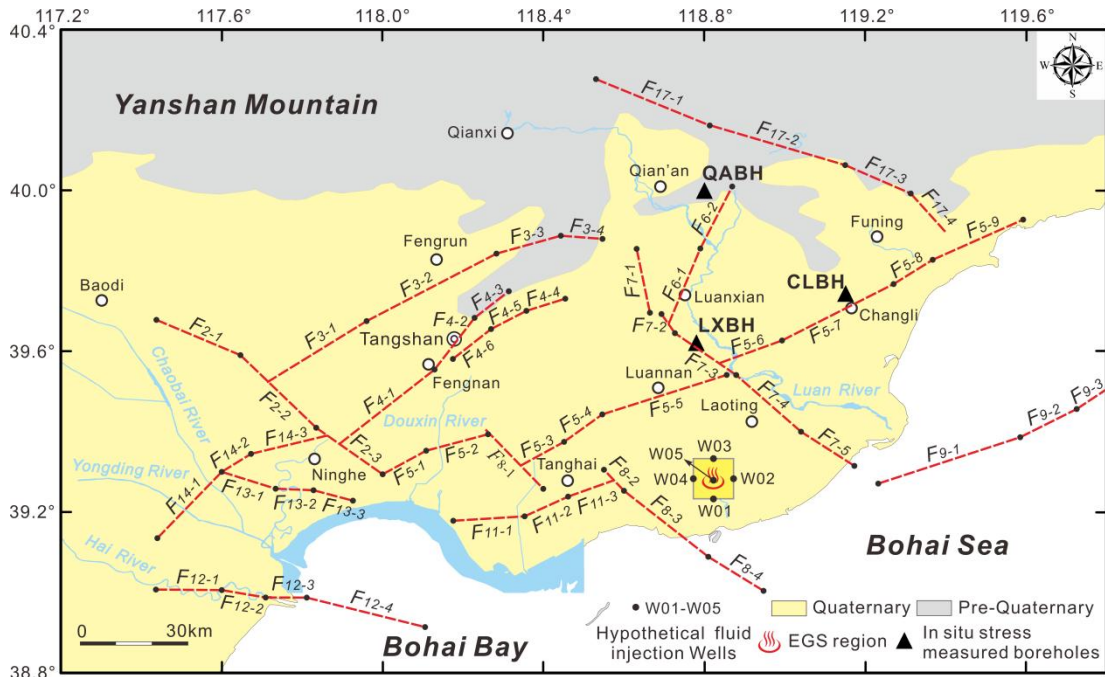
8



9

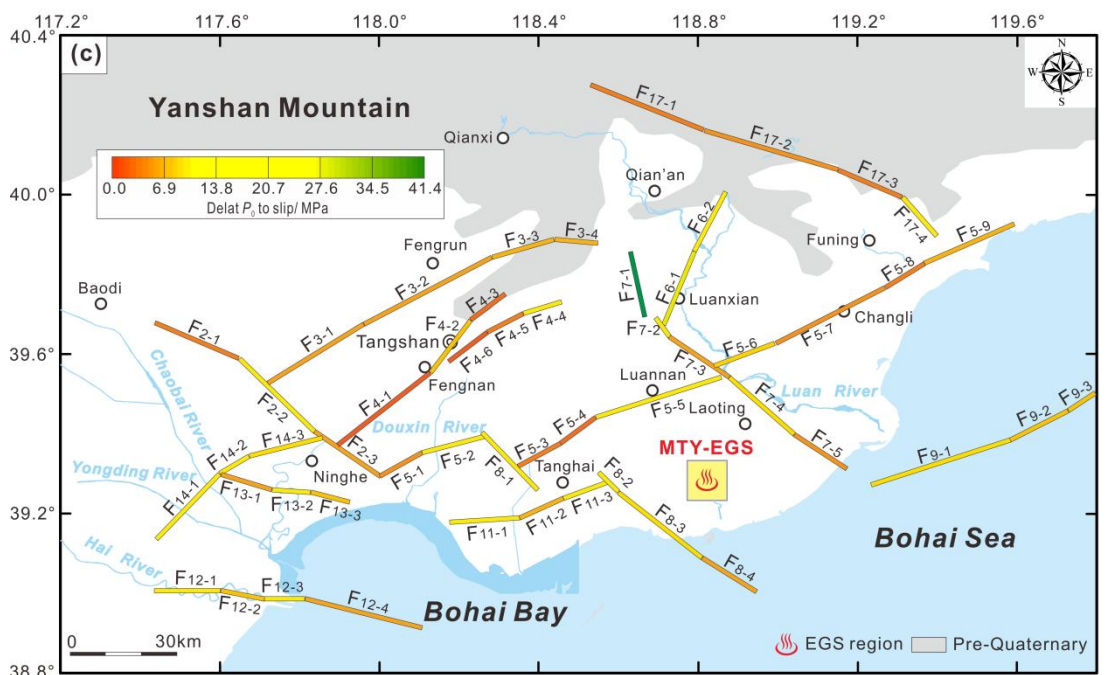
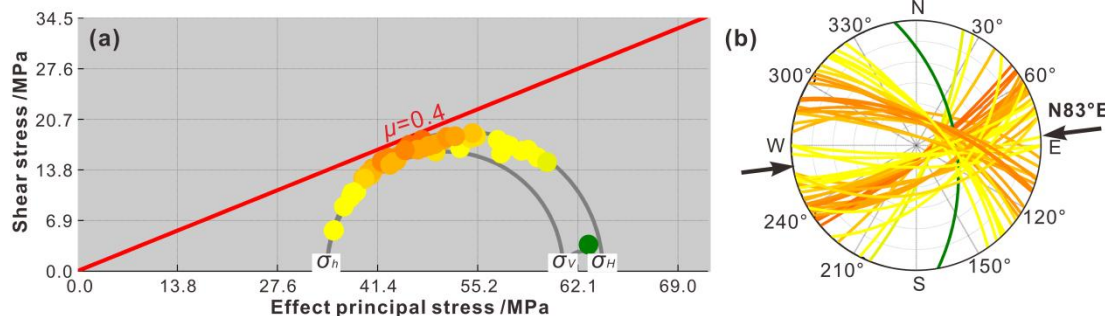
10 **Figure 5.** Hydraulic fracturing in situ stress results at shallow depths (< 1000 m) near the MTY EGS field in
 11 Tangshan seismic region. **(a)** The magnitudes of three principal stresses with the depth. **(b)** The orientations of the
 12 maximum horizontal principal stress (σ_H).

13



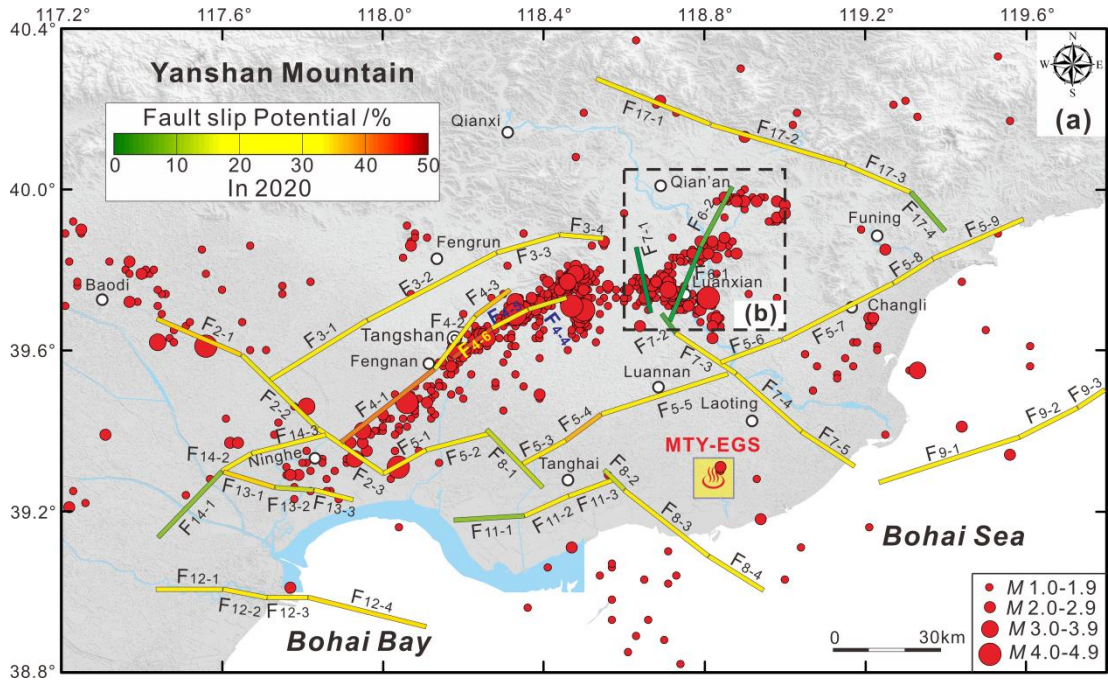
1
2
3
4
5

Figure 6. Simplified-segmental faults with different strikes in the Tangshan seismic region. There are total 53 segments used for calculating the fault slip potential (FSP).

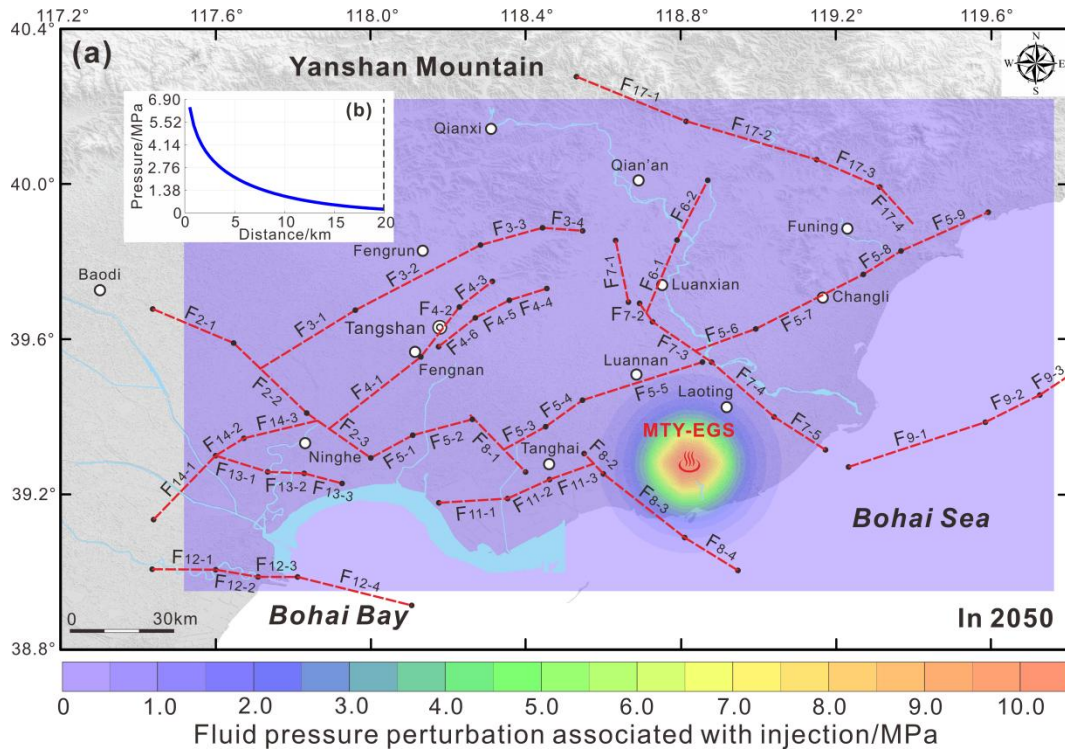


6

1 **Figure 7.** The results of a deterministic geomechanical assessment of fault pore pressure to slip across the
 2 Tangshan seismic region. **(a)** The faults shown on a Mohr diagram, with effective compressive stress on the
 3 horizontal axis and shear stress on the vertical axis; Principal stresses are labeled in black, and the frictional slip
 4 line is shown in red. Faults are colored by their horizontal distance to slip in MPa (according to the color scale). **(b)**
 5 Fault normal orientations plotted on a lower hemisphere equal angle stereonet as arcs; The azimuth of maximum
 6 horizontal compression is shown with black arrows. **(c)** The same faults mapped and colored by deterministic fluid
 7 pore pressure to slip.
 8
 9

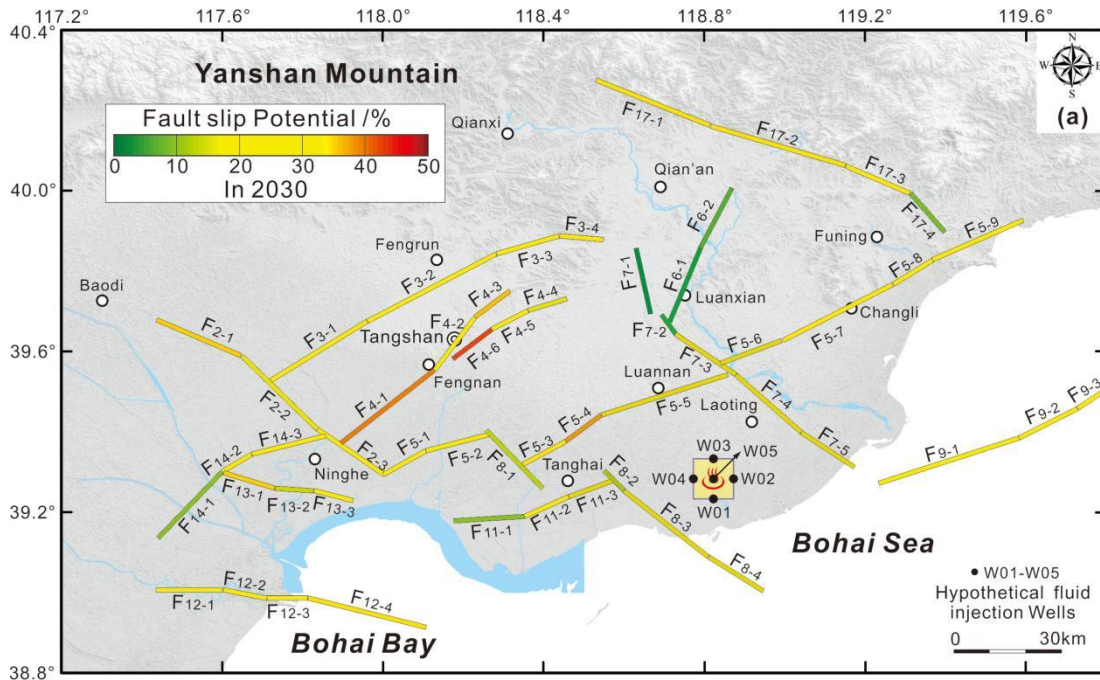


10 **Figure 8.** The probabilistic fault slip potential on the mapped faults without any fluid pressure perturbation in 2020
 11 and the recent earthquakes (2009-2019) with the magnitude of M 1.0-4.9 in Tangshan seismic region (National
 12 Earthquake Data Center, China).
 13

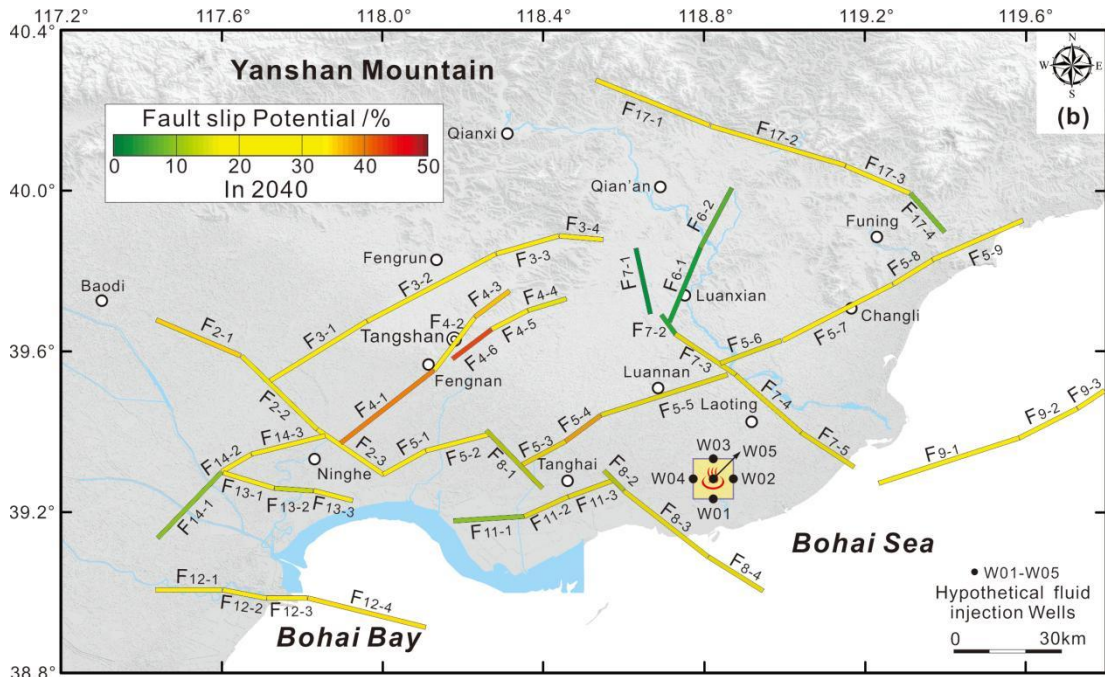


1
2
3
4
5
6

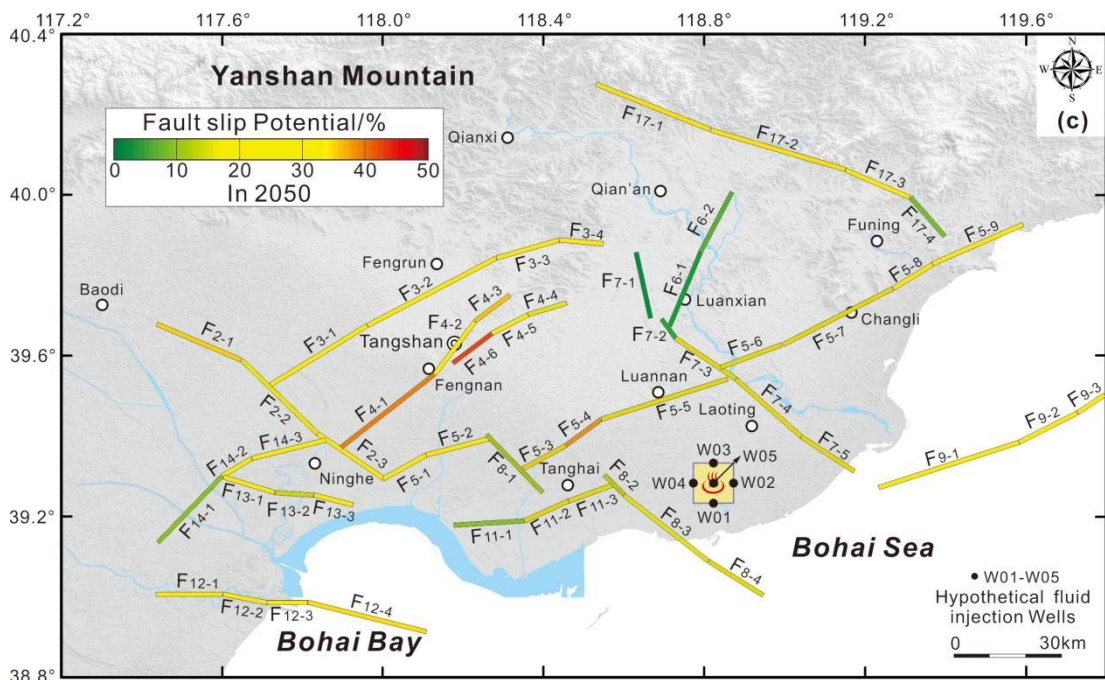
Figure 9. (a) Fluid pressure perturbations from five injection wells linearly superposed onto the mapped domain of Tangshan seismic region in 2050. **(b)** Increase in fluid pore pressure above natural levels due to fluid injection in each of the five wells as a function of distance in model year 2050.



7

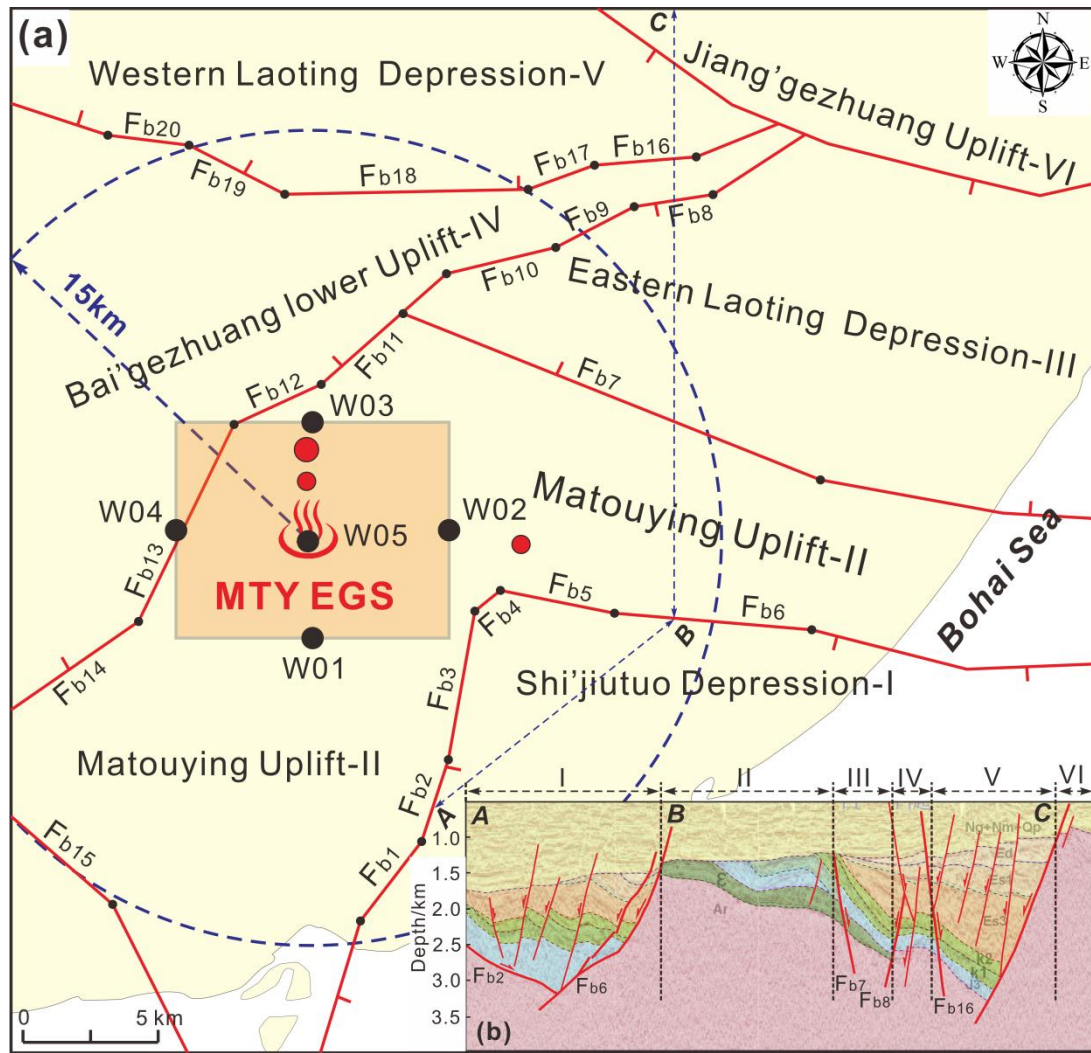


1
2



3
4
5

Figure 10. The probabilistic fault slip potential on the mapped faults in response to the hypothetic fluid injection in the MTY EGS field in 2030 (a), 2040 (b) and 2050 (c), respectively.



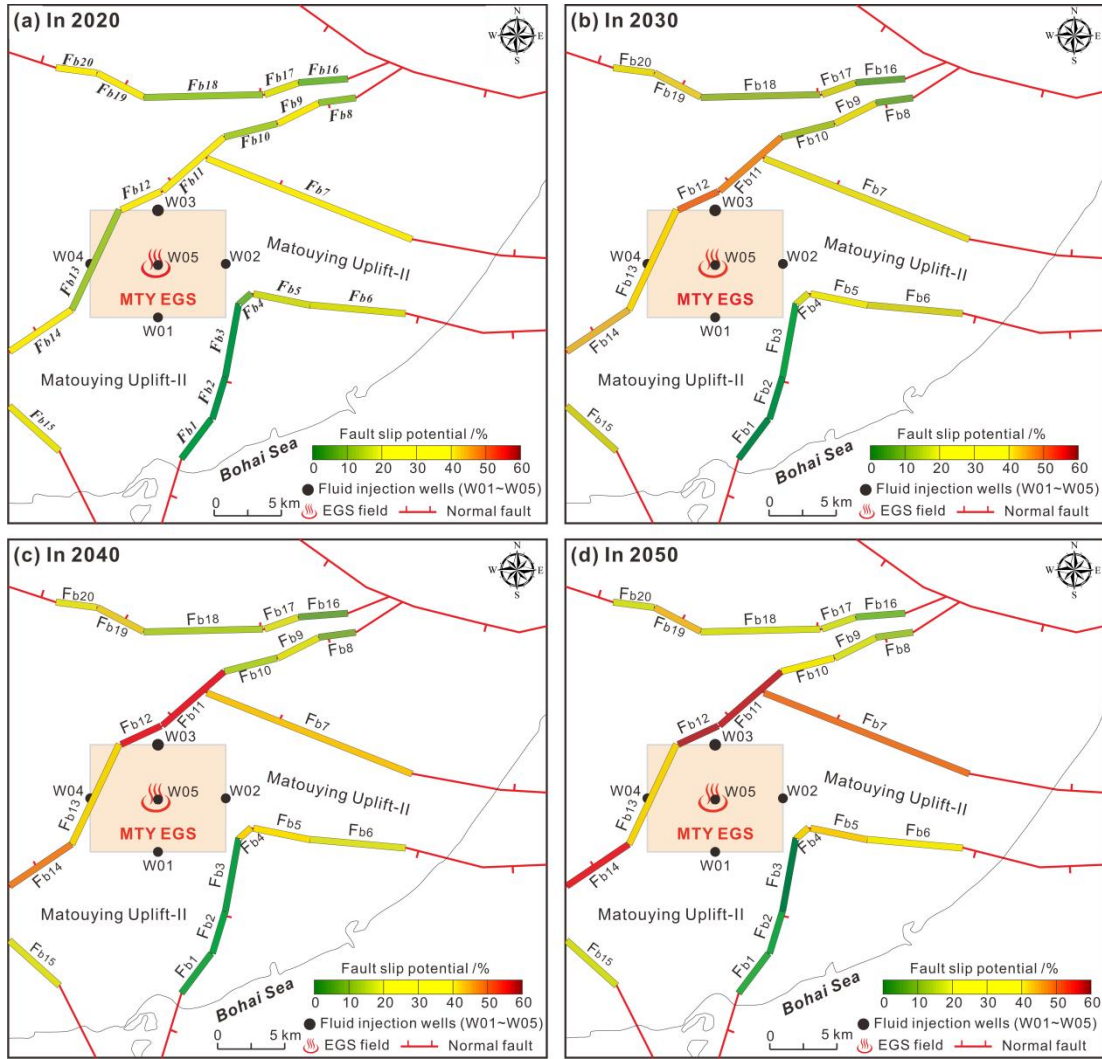
N+Q
 Ed
 Es₁
 Es₃
 K₂
 K₁
 K₁+J₃
 J₃
 E
 Ar

M 2.0-2.9
 M 1.0-1.9
 Injection wells (W01~W05)
 EGS field
 Normal fault

Figure 11. (a) Geological structures and active faults within a range of ~15-20 km away from the MTY EGS field.

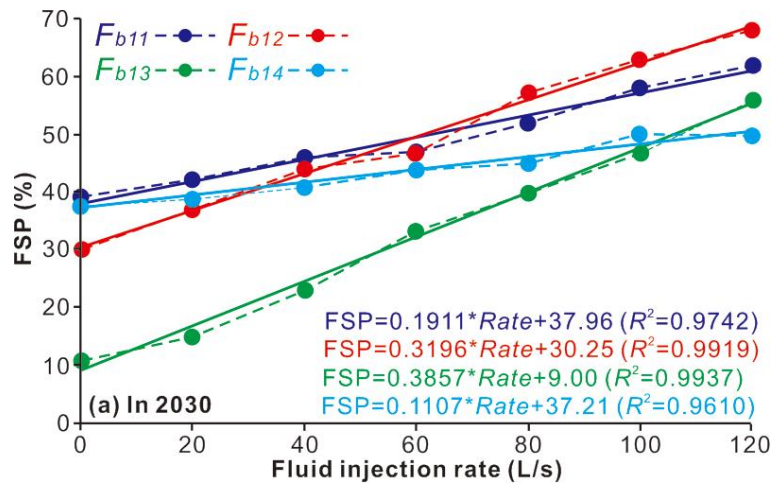
(b) The structural framework of the Matouying uplift and its vicinity from integrated seismic and geological data interpretation.

1
2
3
4
5



1
2 **Figure 12.** The probabilistic fault slip potential on the mapped faults within a range of ~15-20 km away from the
3 MTY EGS field in response of the hypothetical fluid injection in 2020 (a), 2030 (b), 2040 (c) and 2050 (d),
4 respectively.

5
6
7



8

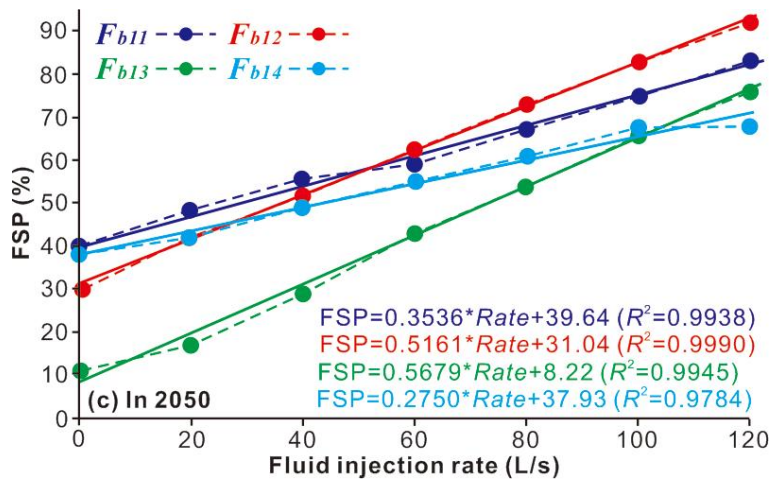
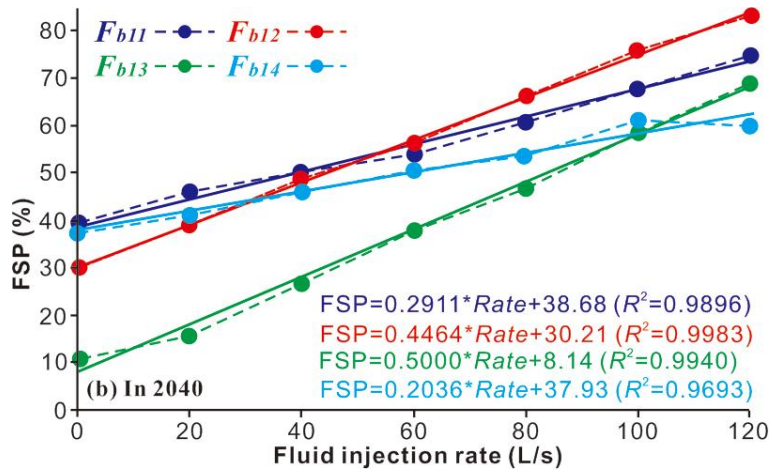
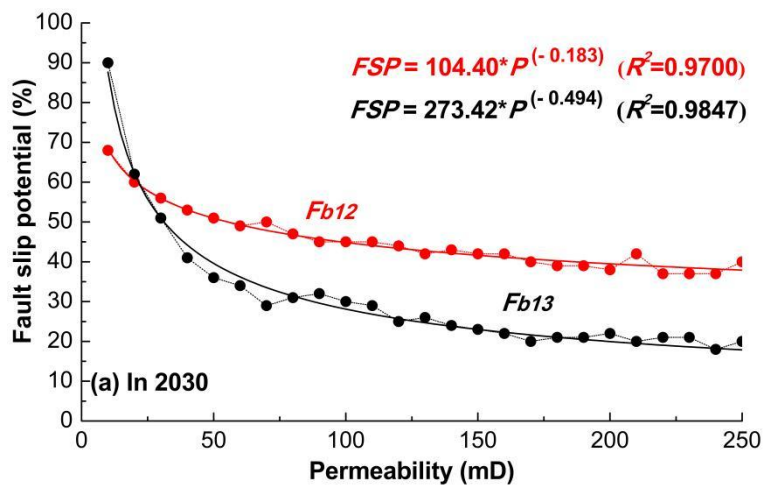


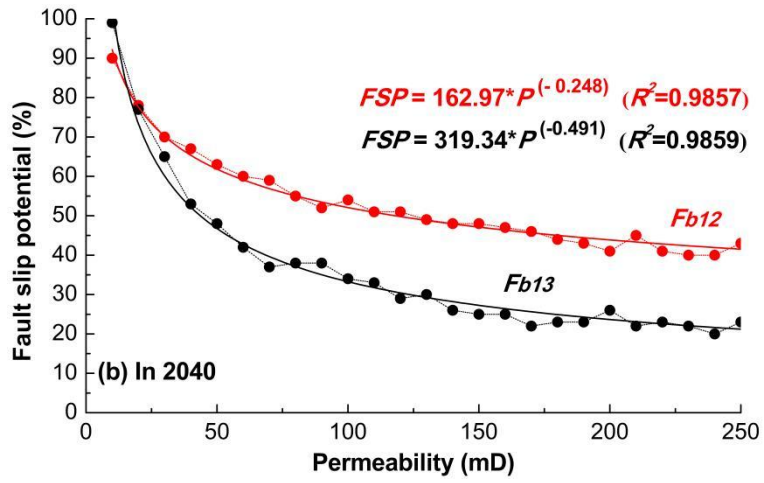
Figure 13. The effect of injection rate on probabilistic fault slip potential on the mapped faults F_{b11} , F_{b12} , F_{b13} , and F_{b14} , within a range of ~ 6-10 km away from the MTY EGS field.



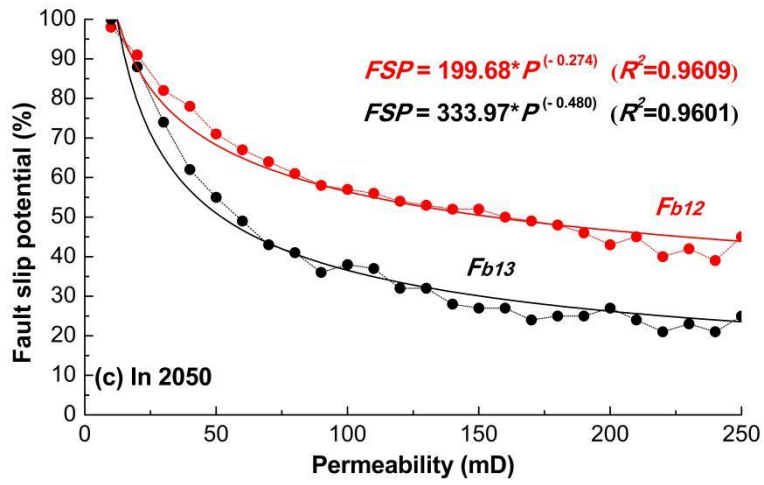
1
2

3
4
5
6
7
8

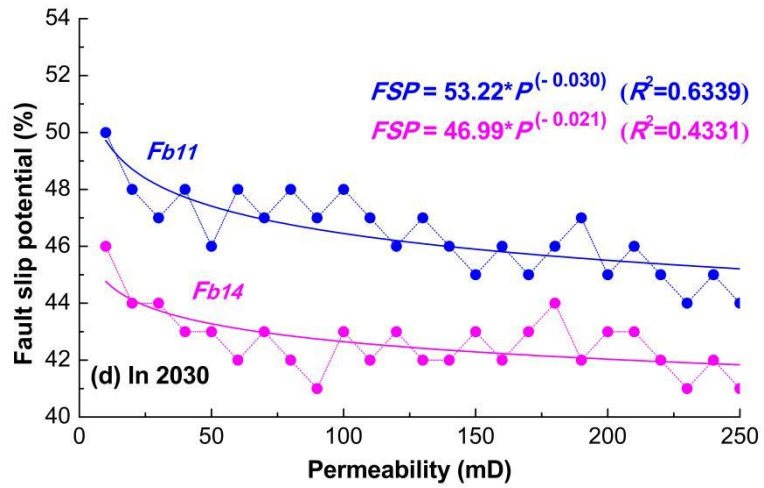
9



1



2



3

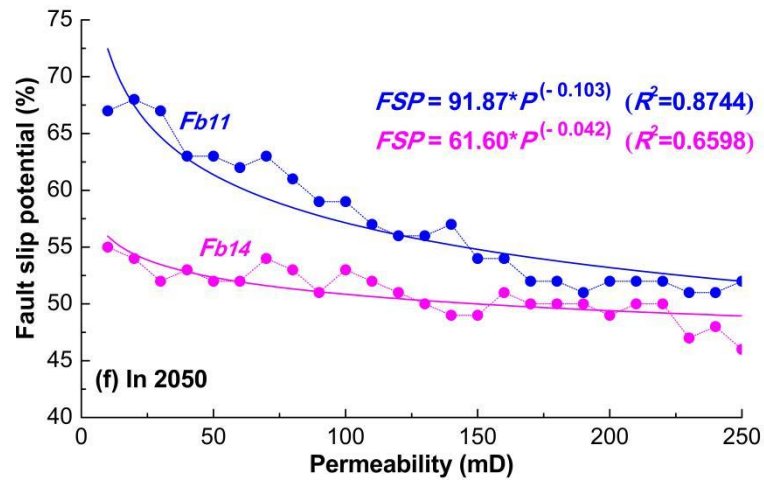
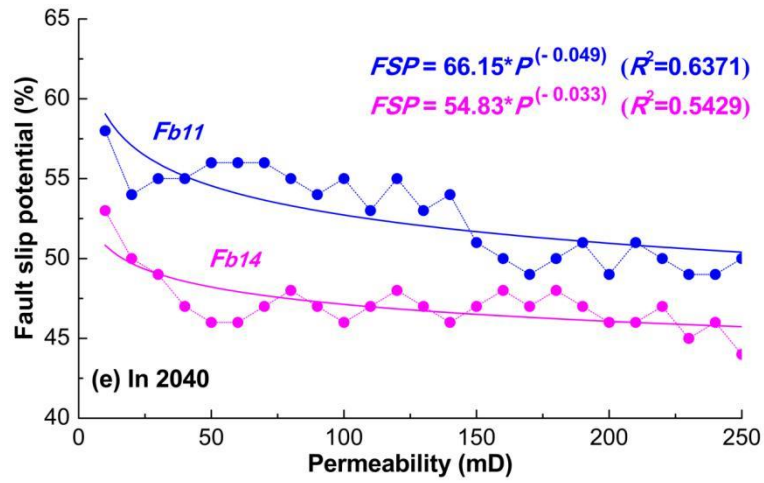
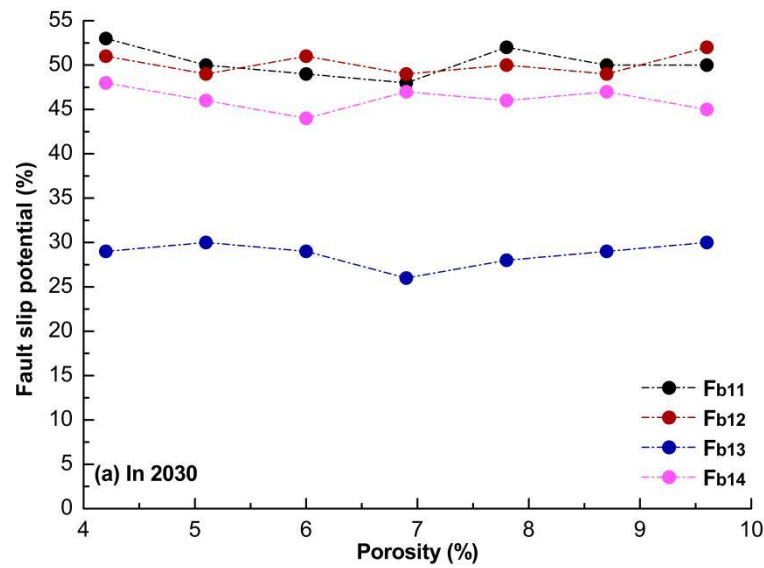
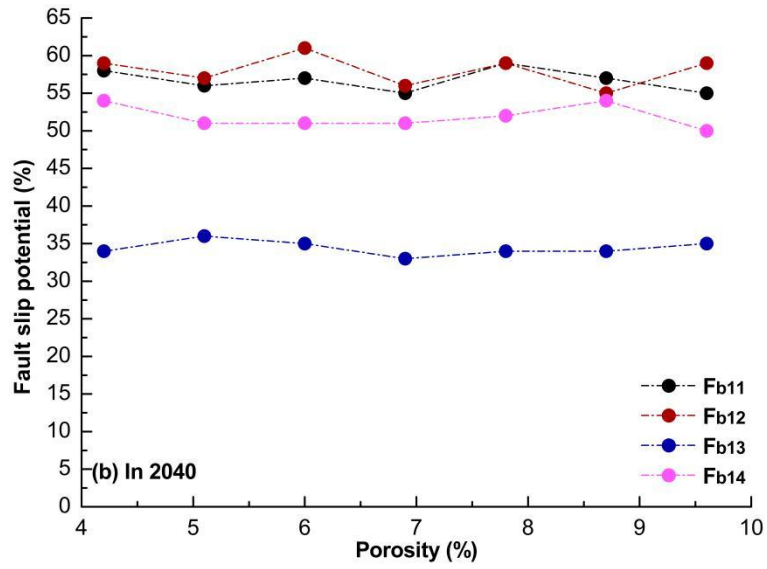
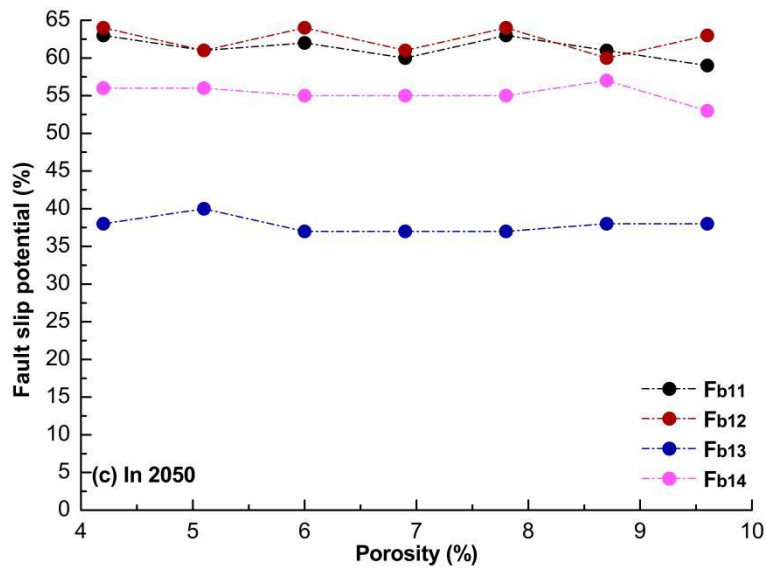


Figure 14. The effect of permeability on probabilistic fault slip potential on the mapped faults F_{b11} , F_{b12} , F_{b13} , and F_{b14} , within a range of ~ 6-10 km away from the MTY EGS field.





1



2

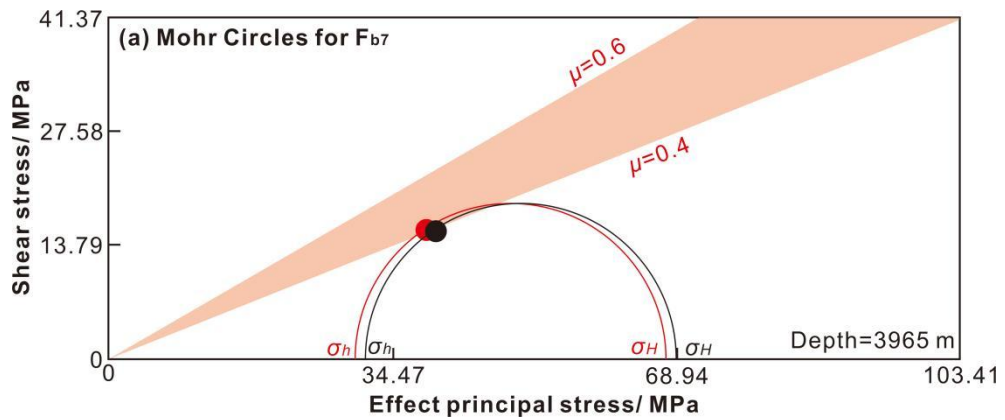
3

Figure 15. The effect of porosity on probabilistic fault slip potential on the mapped faults F_{b11} , F_{b12} , F_{b13} , and F_{b14} , within a range of ~ 6-10 km away from the MTY EGS field.

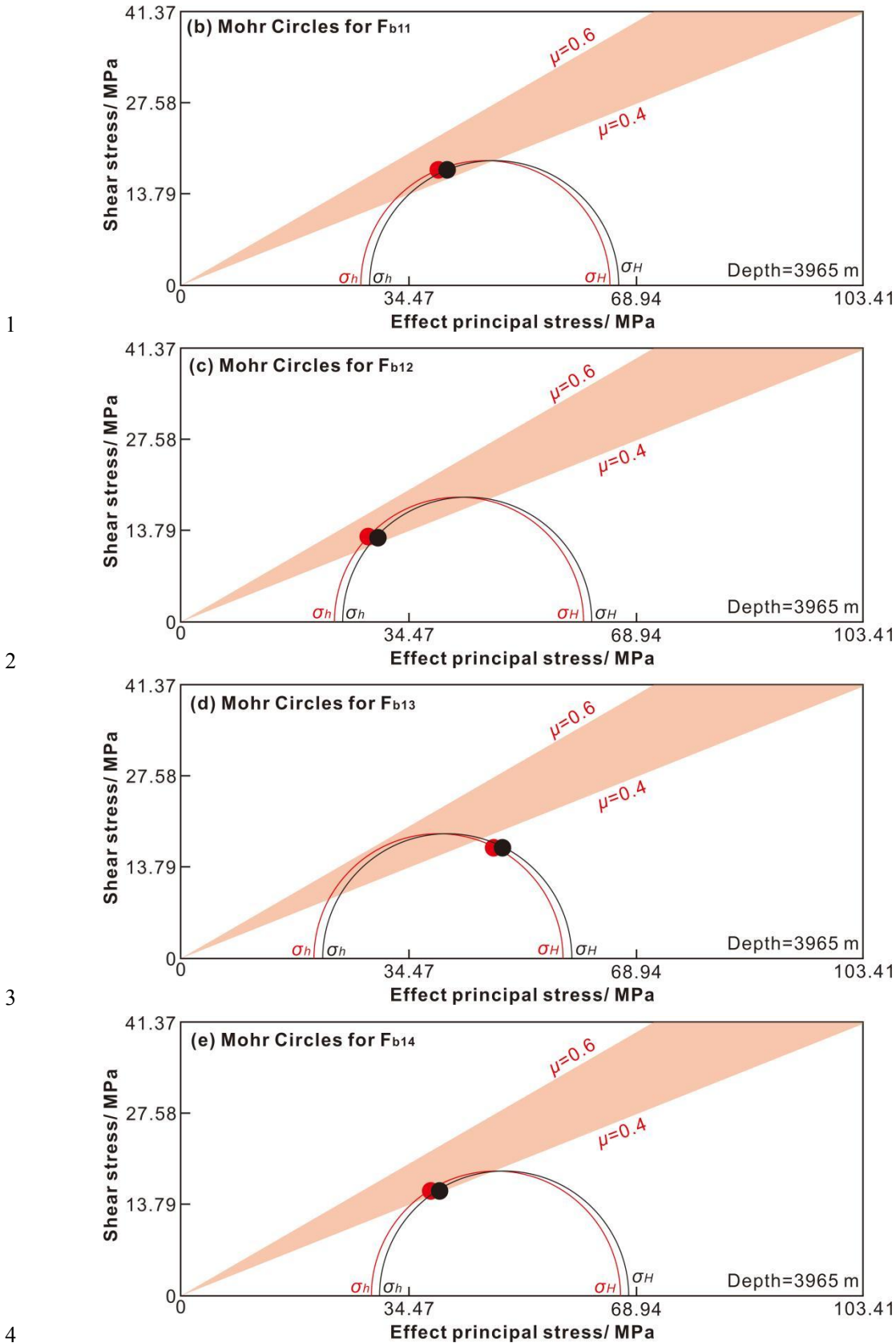
4

5

6



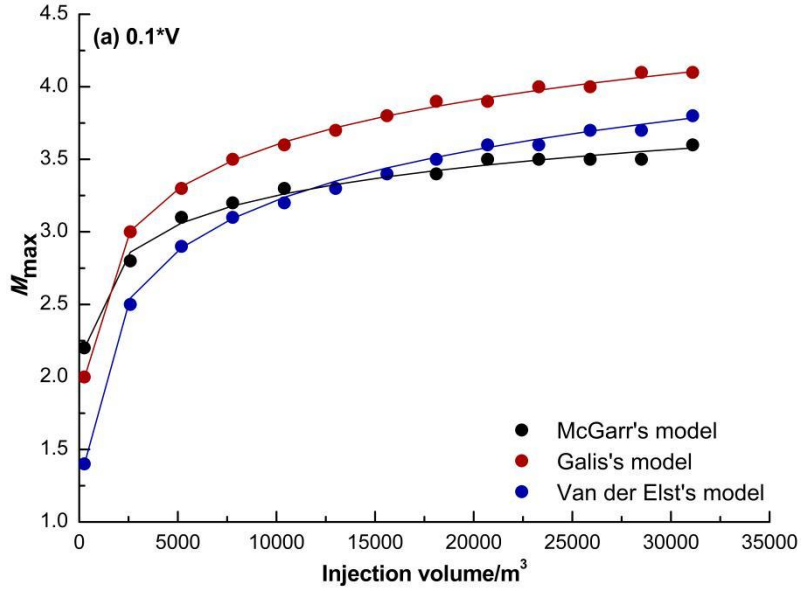
7



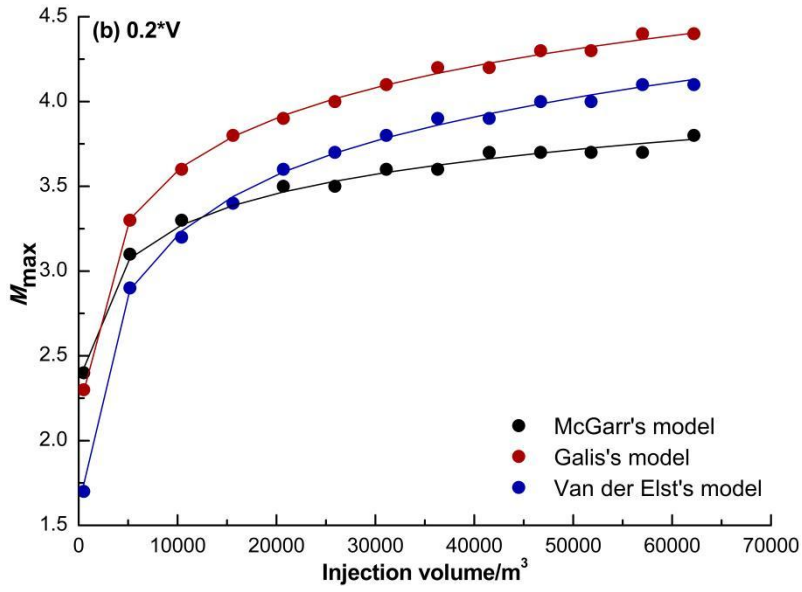
5 **Figure 16.** The effect of thermoelastic stress on fault instability of the mapped faults F_{b11} , F_{b12} , F_{b13} and F_{b14} ,
 6 within a range of ~ 6-10 km away from the MTY EGS field. The changes in horizontal stress is calculated for a
 7 temperature drop of 6°C with a value of 1.25 MPa. The black dot marks the traction of fault instability (a

1 horizontal distance to slip in MPa) without the influence of thermoelastic stress, while the red dot marks the
2 traction of the fault instability with the effect of temperature-induced stress changes.

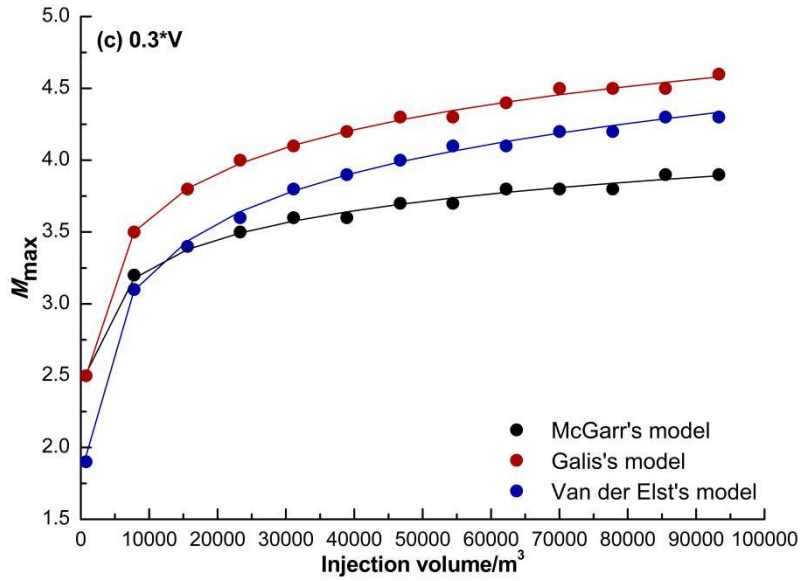
3
4
5



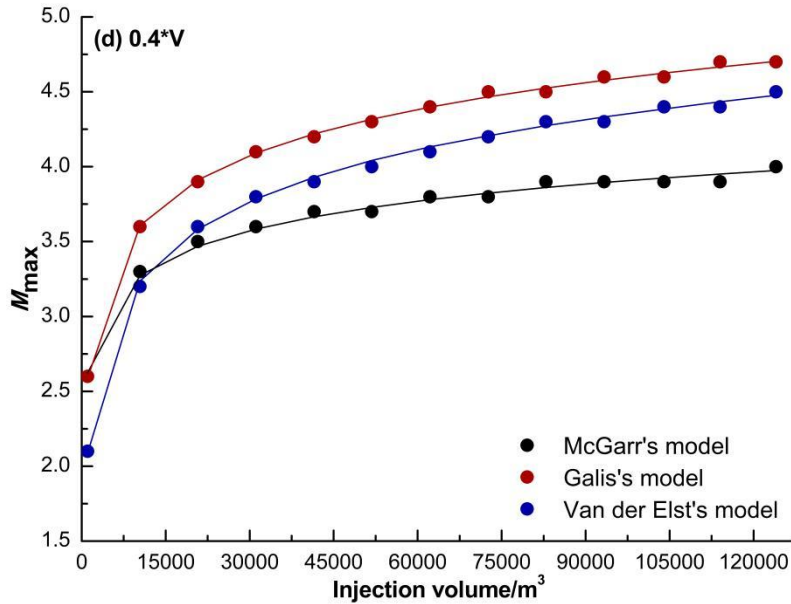
6



7
8
9



1



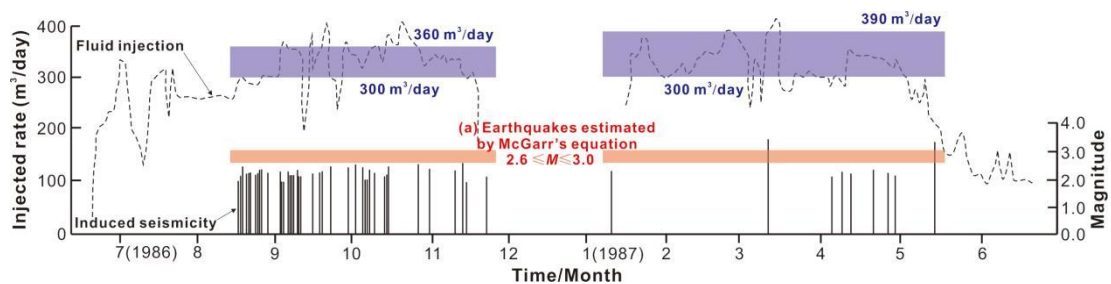
2

3 **Figure 17.** The maximum moment magnitude of injection-induced seismicity within ~10-15 km away from the
 4 injected wells in response to monthly time series of injection volume in MTY EGS field. In the calculation, the
 5 monthly injection volumes (V) are taken as $2.59 \times 10^3 \text{ m}^3$, $2.59 \times 10^4 \text{ m}^3$, $5.18 \times 10^4 \text{ m}^3$, $7.78 \times 10^4 \text{ m}^3$, $1.04 \times 10^5 \text{ m}^3$,
 6 $1.30 \times 10^5 \text{ m}^3$, $1.56 \times 10^5 \text{ m}^3$, $1.81 \times 10^5 \text{ m}^3$, $2.07 \times 10^5 \text{ m}^3$, $2.33 \times 10^5 \text{ m}^3$, $2.59 \times 10^5 \text{ m}^3$, $2.85 \times 10^5 \text{ m}^3$ and $3.11 \times 10^5 \text{ m}^3$,
 7 respectively, corresponding to fluid injected rate of 1 L/s, 10 L/s, 20 L/s, 30 L/s, 40 L/s, 50 L/s, 60 L/s, 70 L/s, 80
 8 L/s, 90 L/s, 100 L/s, 110 L/s and 120 L/s, respectively.

9

10

11



12

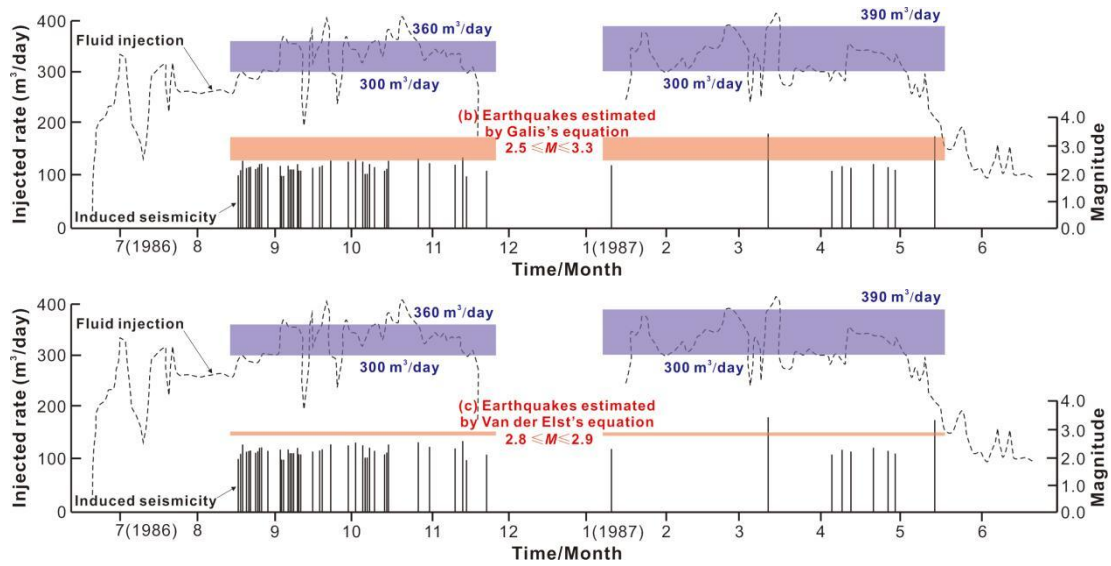


Figure 18. Comparisons of the magnitudes of the injection-induced earthquakes between the observations (black vertical lines) (Zhao and Yang, 1990) and the predicted (pink rectangle) results calculated using the McGarr's model (a), the Galis's model (b), and the Van der Elst's model (c) in the Renqiu oilfield of North China.

Table 1. General conditions of three in situ stress boreholes measured in Tangshan seismic region.

Name	Latitude,N	Longitude,E	Altitude,m	Depth,m	Rock type and integrity
QABH	40.12°	118.81°	38	600	Being fine grained quartzite of the Archean and relatively intact.
CLBH	39.74°	119.15°	56	600	Being medium-coarse grained adamellite of the late Yanshanian Stage and well intact.
LXBH	39.62°	118.78°	39	1000	Being biotite leptynite and locally intercalated with some magnetite quartzite of the Archean, and relatively intact.

Table 2. Hydraulic fracturing in situ stress results at QABH, CLBH, and LXBH boreholes near the MTY EGS field.

Name	Depth, m	Hydraulic fracturing parameter, MPa					Principal stress, MPa			Azimuth of σ_H
		P_0	P_b	P_T	P_s	T	σ_H	σ_h	σ_v	
	184.10	1.67	15.36	11.53	8.31	3.83	15.08	8.31	4.88	N47°W
	208.90	1.92	15.16	10.31	7.40	4.85	13.82	7.40	5.54	/
	212.92	1.96	11.57	7.18	6.39	4.39	12.43	5.66	5.64	N82°W
	225.68	2.09	12.09	8.21	7.77	3.88	17.19	7.77	5.98	/
	251.65	2.35	17.16	12.49	9.69	4.67	18.93	9.69	6.67	N57°W
QABH	305.88	2.89	12.67	7.03	6.83	5.64	16.36	6.83	8.11	/
	335.28	3.19	14.92	10.23	9.17	4.69	20.46	9.17	8.88	/
	380.68	3.64	12.71	8.30	7.12	4.41	16.70	7.12	10.09	/
	468.68	4.52	16.85	13.41	10.44	3.44	22.43	10.44	12.42	N78°W
	475.03	4.58	17.93	14.78	12.66	3.15	27.79	12.66	12.59	/
	511.30	4.95	19.68	14.71	12.76	4.97	28.51	12.76	13.55	/

	543.50	5.27	16.69	12.31	11.13	4.38	26.34	11.13	14.40	/
	562.00	5.45	15.84	10.41	9.61	5.43	23.88	9.61	14.89	N62°W
	590.32	5.74	16.08	12.18	10.68	3.90	25.59	10.68	15.64	/
CLBH	79.50	0.70	12.25	7.43	4.63	4.82	5.76	4.63	2.11	N60°E
	94.50	0.85	13.41	7.36	5.62	6.05	8.65	5.62	2.50	/
	119.50	1.10	19.78	6.11	3.75	13.67	4.04	3.75	3.17	/
	137.50	1.28	16.76	6.58	4.14	10.18	4.56	4.14	3.64	/
	206.50	1.97	18.24	6.00	5.20	12.24	7.63	5.20	5.47	N84°E
	248.10	2.38	16.94	6.62	5.56	10.32	7.68	5.56	6.57	/
	255.50	2.46	13.59	5.64	5.17	7.95	7.41	5.17	6.77	/
	290.50	2.81	14.02	7.71	6.18	6.31	8.02	6.18	7.70	N82°W
	335.50	3.26	16.03	8.46	7.75	7.57	11.53	7.75	8.89	/
	365.50	3.56	18.16	9.23	7.34	8.93	9.23	7.34	9.69	N79°E
	390.20	3.80	10.41	7.94	7.13	2.47	9.65	7.13	10.34	/
	393.50	3.94	14.26	9.75	9.18	4.51	13.95	9.18	10.43	/
	476.30	4.66	19.34	13.92	9.87	5.42	11.03	9.87	12.62	/
485.50	4.76	24.65	13.61	10.62	11.04	13.49	10.62	12.87	N55°E	
LXBH	340.00	3.36	21.50	16.26	11.53	5.24	14.97	11.53	9.01	N60°W
	386.00	3.82	24.42	18.82	14.38	5.60	20.50	14.38	10.23	/
	413.50	4.10	30.56	17.59	14.22	12.97	20.97	14.22	10.96	N70°W
	450.78	4.47	28.07	16.65	13.38	11.42	19.02	13.38	11.95	/
	506.00	5.02	28.19	16.89	13.49	11.30	18.56	13.49	13.41	/
	557.00	5.53	25.46	17.55	14.37	7.91	20.03	14.37	14.76	/
	605.00	6.01	24.79	18.05	15.40	6.74	22.14	15.40	16.03	N74°W
	649.26	6.45	26.20	17.97	15.49	8.23	22.05	15.49	17.21	/
	700.00	6.96	28.83	19.61	17.29	9.22	25.30	17.29	18.55	/
	748.00	7.44	29.97	19.00	16.48	10.97	23.00	16.48	19.82	/
	818.00	8.14	27.71	19.76	17.04	7.95	23.22	17.04	21.68	/
922.44	9.18	27.70	20.96	19.46	6.84	28.24	19.46	24.44	/	

1 Being noted that: P_b , P_r , and P_s denote the breakdown, reopening and shut-in pressure, respectively. σ_H , σ_h , and σ_v
2 denote the maximum, minimum horizontal and vertical principal stresses, respectively. P_0 is the natural pore
3 pressure, and T indicates the tensile strength of rock being equal to the difference between P_b and P_r .

4

5 **Table 3.** The tensorial mean of hydraulic fracturing in situ stress results at similar depths in three boreholes near
6 the MTY EGS field.

Name	Depth, m	In situ stress measured results, MPa			Average azimuth	In situ stress tensors, MPa			Tensorial mean of in situ stress, MPa			Estimated azimuth of σ_H
		σ_H	σ_h	Azimuth of σ_H		σ_{xx}	σ_{yy}	σ_{xy}	σ^a_{xx}	σ^a_{yy}	σ^a_{xy}	
QABH	212.92	12.43	5.66	98°	91°	12.30	5.79	0.93	9.95	5.51	0.34	86°
CLBH	206.50	7.63	5.20	84°		7.60	5.23	-0.25				
LXBH	340.00	14.97	11.53	120°	99.5°	14.11	12.39	1.49	11.64	9.90	0.57	73°
CLBH	365.50	9.23	7.34	79°		9.16	7.41	-0.35				
QABH	468.68	22.43	10.44	102°	78.5°	21.91	10.96	2.44	17.23	11.26	0.54	85°

1 Being noted that: Normal compressive stress is defined as positive, while tensional stress is negative. Shear stress
 2 is positive (block clockwise rotation). For the x - o - y coordinate system, the positive direction of the x -axis and
 3 y -axis are the same as the azimuth of East (E) and North (N), respectively.

4

5 **Table 4.** The geological information of the main active faults used for calculating probabilistic fault slip potential
 6 in the Tangshan seismic region.

Name	Segment	Length, km	strike	dip	Coefficient of friction
Jiyunhe fault (F_2)	F_{2-1}	25.37	292°±5°	70°±10°	0.4±0.05
	F_{2-2}	29.37	315°±5°	70°±10°	0.4±0.05
	F_{2-3}	22.25	305°±5°	70°±10°	0.4±0.05
Yejituo fault (F_3)	F_{3-1}	32.04	58°±5°	60°±10°	0.4±0.05
	F_{3-2}	40.50	62°±5°	60°±10°	0.4±0.05
	F_{3-3}	18.69	77°±5°	60°±10°	0.4±0.05
	F_{3-4}	12.02	276°±5°	60°±10°	0.4±0.05
Tangshan fault belt (F_4)	F_{4-1}	33.38	50°±5°	80°±10°	0.4±0.05
	F_{4-2}	18.47	39°±5°	80°±10°	0.4±0.05
	F_{4-3}	12.02	53°±5°	80°±10°	0.4±0.05
	F_{4-4}	11.57	74°±5°	80°±10°	0.4±0.05
	F_{4-5}	11.13	60°±5°	80°±10°	0.4±0.05
	F_{4-6}	13.80	50°±5°	80°±10°	0.4±0.05
Changli-Ninghe fault (F_5)	F_{5-1}	13.80	62°±5°	75°±10°	0.4±0.05
	F_{5-2}	17.80	75°±5°	75°±10°	0.4±0.05
	F_{5-3}	13.57	60°±5°	75°±10°	0.4±0.05
	F_{5-4}	13.13	54°±5°	75°±10°	0.4±0.05
	F_{5-5}	36.05	73°±5°	75°±10°	0.4±0.05
	F_{5-6}	18.47	68°±5°	75°±10°	0.4±0.05
	F_{5-7}	34.71	62°±5°	75°±10°	0.4±0.05
	F_{5-8}	12.91	60°±5°	75°±10°	0.4±0.05
	F_{5-9}	27.59	65°±5°	75°±10°	0.4±0.05
Lulong fault (F_6)	F_{6-1}	22.92	22°±5°	75°±10°	0.4±0.05
	F_{6-2}	19.58	27°±5°	75°±10°	0.4±0.05
Luanxian-Laoting fault (F_7)	F_{7-1}	18.25	350°±5°	70°±10°	0.4±0.05
	F_{7-2}	6.68	325°±5°	70°±10°	0.4±0.05
	F_{7-3}	20.69	305°±5°	70°±10°	0.4±0.05
	F_{7-4}	24.03	310°±5°	70°±10°	0.4±0.05
	F_{7-5}	17.80	303°±5°	70°±10°	0.4±0.05
Baigezhuang fault (F_8)	F_{8-1}	22.70	317°±5°	65°±10°	0.4±0.05
	F_{8-2}	8.46	316°±5°	65°±10°	0.4±0.05
	F_{8-3}	29.37	307°±5°	65°±10°	0.4±0.05
	F_{8-4}	18.25	300°±5°	65°±10°	0.4±0.05
Qinbei fault (F_9)	F_{9-1}	41.39	72°±5°	60°±10°	0.4±0.05
	F_{9-2}	17.80	60°±5°	60°±10°	0.4±0.05
	F_{9-3}	9.79	56°±5°	60°±10°	0.4±0.05

Xi'nanzhuang fault (F_{11})	F_{11-1}	20.03	$86^{\circ}\pm 5^{\circ}$	$80^{\circ}\pm 10^{\circ}$	0.4 ± 0.05
	F_{11-2}	13.35	$64^{\circ}\pm 5^{\circ}$	$80^{\circ}\pm 10^{\circ}$	0.4 ± 0.05
	F_{11-3}	13.35	$70^{\circ}\pm 5^{\circ}$	$80^{\circ}\pm 10^{\circ}$	0.4 ± 0.05
Haihe fault (F_{12})	F_{12-1}	18.25	$90^{\circ}\pm 5^{\circ}$	$70^{\circ}\pm 10^{\circ}$	0.4 ± 0.05
	F_{12-2}	12.46	$280^{\circ}\pm 5^{\circ}$	$70^{\circ}\pm 10^{\circ}$	0.4 ± 0.05
	F_{12-3}	11.13	$90^{\circ}\pm 5^{\circ}$	$70^{\circ}\pm 10^{\circ}$	0.4 ± 0.05
	F_{12-4}	33.82	$285^{\circ}\pm 5^{\circ}$	$70^{\circ}\pm 10^{\circ}$	0.4 ± 0.05
Hangu fault (F_{13})	F_{13-1}	15.58	$288^{\circ}\pm 5^{\circ}$	$82^{\circ}\pm 10^{\circ}$	0.4 ± 0.05
	F_{13-2}	10.68	$90^{\circ}\pm 5^{\circ}$	$82^{\circ}\pm 10^{\circ}$	0.4 ± 0.05
	F_{13-3}	11.57	$285^{\circ}\pm 5^{\circ}$	$82^{\circ}\pm 10^{\circ}$	0.4 ± 0.05
Cangdong fault (F_{14})	F_{14-1}	25.81	$43^{\circ}\pm 5^{\circ}$	$48^{\circ}\pm 10^{\circ}$	0.4 ± 0.05
	F_{14-2}	9.79	$60^{\circ}\pm 5^{\circ}$	$48^{\circ}\pm 10^{\circ}$	0.4 ± 0.05
	F_{14-3}	21.81	$77^{\circ}\pm 5^{\circ}$	$48^{\circ}\pm 10^{\circ}$	0.4 ± 0.05
Lengkou fault (F_{17})	F_{17-1}	34.27	$291^{\circ}\pm 5^{\circ}$	$65^{\circ}\pm 10^{\circ}$	0.4 ± 0.05
	F_{17-2}	39.16	$286^{\circ}\pm 5^{\circ}$	$65^{\circ}\pm 10^{\circ}$	0.4 ± 0.05
	F_{17-3}	20.03	$292^{\circ}\pm 5^{\circ}$	$65^{\circ}\pm 10^{\circ}$	0.4 ± 0.05
	F_{17-4}	14.24	$320^{\circ}\pm 5^{\circ}$	$65^{\circ}\pm 10^{\circ}$	0.4 ± 0.05

1

2

3

Table 5. The geological information of the main boundary faults used for calculating probabilistic fault slip potential in the MTY EGS field.

4

Tectonic units	Segment	Length/km	strike	dip	Coefficient of the friction
Between II and I	F_{b1}	3.85	$35^{\circ}\pm 5^{\circ}$	$45^{\circ}\pm 10^{\circ}$	0.4 ± 0.05
	F_{b2}	3.21	$20^{\circ}\pm 5^{\circ}$	$45^{\circ}\pm 10^{\circ}$	0.4 ± 0.05
	F_{b3}	5.64	$10^{\circ}\pm 5^{\circ}$	$45^{\circ}\pm 10^{\circ}$	0.4 ± 0.05
	F_{b4}	1.28	$50^{\circ}\pm 5^{\circ}$	$45^{\circ}\pm 10^{\circ}$	0.4 ± 0.05
	F_{b5}	4.36	$100^{\circ}\pm 5^{\circ}$	$45^{\circ}\pm 10^{\circ}$	0.4 ± 0.05
	F_{b6}	7.56	$95^{\circ}\pm 5^{\circ}$	$45^{\circ}\pm 10^{\circ}$	0.4 ± 0.05
Between II and III	F_{b7}	16.67	$110^{\circ}\pm 5^{\circ}$	$80^{\circ}\pm 10^{\circ}$	0.4 ± 0.05
Between III and IV	F_{b8}	3.08	$80^{\circ}\pm 5^{\circ}$	$80^{\circ}\pm 10^{\circ}$	0.4 ± 0.05
	F_{b9}	3.33	$60^{\circ}\pm 5^{\circ}$	$80^{\circ}\pm 10^{\circ}$	0.4 ± 0.05
	F_{b10}	4.23	$76^{\circ}\pm 5^{\circ}$	$80^{\circ}\pm 10^{\circ}$	0.4 ± 0.05
Between II and IV	F_{b11}	6.15	$50^{\circ}\pm 5^{\circ}$	$80^{\circ}\pm 10^{\circ}$	0.4 ± 0.05
	F_{b12}	3.72	$63^{\circ}\pm 5^{\circ}$	$80^{\circ}\pm 10^{\circ}$	0.4 ± 0.05
	F_{b13}	8.21	$25^{\circ}\pm 5^{\circ}$	$80^{\circ}\pm 10^{\circ}$	0.4 ± 0.05
	F_{b14}	5.77	$55^{\circ}\pm 5^{\circ}$	$80^{\circ}\pm 10^{\circ}$	0.4 ± 0.05
Southwestern II	F_{b15}	4.87	$130^{\circ}\pm 5^{\circ}$	$65^{\circ}\pm 10^{\circ}$	0.4 ± 0.05
Between IV and V	F_{b16}	3.85	$84^{\circ}\pm 5^{\circ}$	$80^{\circ}\pm 10^{\circ}$	0.4 ± 0.05
	F_{b17}	2.69	$70^{\circ}\pm 5^{\circ}$	$80^{\circ}\pm 10^{\circ}$	0.4 ± 0.05
	F_{b18}	9.10	$90^{\circ}\pm 5^{\circ}$	$80^{\circ}\pm 10^{\circ}$	0.4 ± 0.05
	F_{b19}	3.85	$120^{\circ}\pm 5^{\circ}$	$80^{\circ}\pm 10^{\circ}$	0.4 ± 0.05
	F_{b20}	3.08	$97^{\circ}\pm 5^{\circ}$	$80^{\circ}\pm 10^{\circ}$	0.4 ± 0.05

5